

Modelling instantaneous dynamic triggering in a 3-D fault system: application to the 2000 June South Iceland seismic sequence

A. Bizzarri¹ and M. E. Belardinelli²

¹Istituto Nazionale di Geofisica e Vulcanologia, Sezione di Bologna, Bologna, Italy. E-mail: bizzarri@bo.ingv.it

²Università degli Studi di Bologna, Dipartimento di Fisica, Bologna, Italy

Accepted 2008 February 20. Received 2008 February 20; in original form 2007 October 3

SUMMARY

We present a model of seismogenesis on an extended 3-D fault, subject to the external perturbations of coseismic stress changes due to an earthquake occurring on another fault (the causative fault). As an application, we consider the spatio-temporal stress redistribution produced on the Hvalhnúkur fault by the M_S 6.6 2000 June 17 mainshock in the South Iceland Seismic Zone (SISZ). The latter is located nearly 64 km from the causative fault and failed 26 s after the main shock with an estimated magnitude $M_w = 5.25 \pm 0.25$, providing an example of instantaneous dynamic triggering. The stress perturbations are computed by means of a discrete wavenumber and reflectivity code. The response of the perturbed fault is then analysed solving the *truly* 3-D, fully dynamic (or spontaneous) problem accounting for crustal stratification. In a previous study, the response of the Hvalhnúkur fault was analysed by using a spring–slider fault model (SS fault model), comparing the estimated perturbed failure time with the observed origin time. In addition to the perturbed failure time, this model can provide numerical estimates of many other dynamic features of the triggered event, which can be compared with available observations—the rupture history of the whole fault plane, its final extent and the seismic moment of the induced event. We show the key differences existing between a mass–spring model and this extended fault model; in particular, we show the essential role of the load exerted by the neighbouring slipping points of the fault. By considering both rate- and state-dependent laws and non-linear slip-dependent law, we show how the dynamics of the 26 s fault strongly depend on the assumed constitutive law and initial stress conditions. In the case of rate- and state-dependent friction laws, assuming an initial effective normal stress distribution that is suitable for the SISZ and consistent with previously stated conditions of instantaneous dynamic triggering of the Hvalhnúkur fault, we obtain results in general agreement with observations.

Key words: Earthquake dynamics; Earthquake interaction, forecasting, and prediction; Computational seismology; Wave propagation; Rheology and friction of fault zones.

1 INTRODUCTION

Earthquake slip results in a stress redistribution with respect to the initial state of the seismogenic area—a net local shear stress decrease on the fault surface (stress drop) and a variation of the stress tensor components in the surrounding medium caused by the propagation of seismic waves. In particular, stress increase can cause further earthquakes or aftershocks.

In spite of the logical and apparent simplicity of the above-mentioned mechanism, fault triggering is not a well-understood phenomenon. First of all, it has not been observed as widely as expected (King *et al.* 1994). Moreover, impeding understanding of this mechanism, there is a general ignorance about the initial state of fault(s)—in term of pre-stress, fault surface geometry and segmentation, initial sliding velocity, etc.—and several uncertainties about the physical processes occurring during faulting or, in other words, the ignorance about the most proper analytical form of the governing law describing the processes.

In this paper we will focus on the so-called instantaneous (or immediate) dynamic triggering, that is, a kind of dynamic triggering that is realized after the arrival of the seismic waves of the causative event in the location of the triggered event and within the wave train duration (e.g. Belardinelli *et al.* 2003; Ziv 2006). Static triggering is not suitable to interpret this kind of fault interaction because it occurs before the static level of stress changes. The triggering effect considered in this work occurs in a temporal interval of tens of seconds and in a spatial distance of several tens of kilometres from the causative event.

Remote triggering is a case of dynamic triggering occurring at distances larger than the dimension of the causative fault. In these conditions, the transient stress perturbations are dominant with respect to the static (or permanent) stress changes, leading to static triggering (see for instance Rybicki *et al.* 1985; Cotton & Coutant 1997; Gomberg *et al.* 1997, 1998). Since the M_w 7.3 1992 Landers earthquake, only a few examples of remote triggering of earthquakes have been observed: M_w 5.4 1992 Roermond EQ (Camelbeeck

et al. 1994), M_w 7.1 1999 Hector Mine EQ (Gomberg *et al.* 2001), M_S 7.6 1988 Gulf of Alaska EQ, M_S 7.1 1989 Loma Prieta EQ (Stark & Davis 1996), M_w 7.4 1999 Izmit EQ (Brodsky *et al.* 2000) and M_w 7.9 2002 Denali EQ (Eberhart-Phillips *et al.* 2003). The two early events in Reykjanes Peninsula of the 2000 June 17 seismic sequence in the South Iceland Seismic Zone (SISZ) fall into this small class of examples.

The 2000 June 17 seismic sequence took place in the SISZ and in the Reykjanes Peninsula (hereafter RP) starting in June 2000 (see Fig. 1). It was very well monitored by different local networks: strong motion network, volumetric strain meter networks, digital seismic stations and permanent GPS stations (Árnadóttir *et al.* 2000, 2001, 2004). We recall here only a few features of this sequence, as all the details are given in a previous paper [Antonioli *et al.* 2006 (hereafter AEA06)] and references therein. The sequence started on June 17, at 15:40:41 UTC (this corrects a misprint in AEA06), with an event of magnitude $M_S = 6.6$ (Pedersen *et al.* 2001), with hypocentre located at the absolute coordinates of (63.973°N, 20.367°W, 6.3 km) (Stefánsson *et al.* 2003; Árnadóttir *et al.* 2006). Three early events occurred along the SISZ and its prolongation along the RP at 8 s (M_L 3.5), 26 s ($M_L = 5.5$) and 30 s ($M_L = 5.5$) after the June 17 main shock, respectively. The 26 and 30 s events are associated to the arrival of the shear waves of the main shock (Vogfjörð 2003).

Conditions to have instantaneous dynamic triggering of these three events were found by AEA06 using a simple 1-D spring-slider analogue model (SS analogue model) of perturbed fault and comparing the modelled failure times with the observed origin times. Of these three events, the 26 s event is the best constrained from seismological observations, and therefore in the following of this study we will focus on this aftershock, which occurred on

the Hvalhnúkur fault (HV in Fig. 1). Its hypocentre is located at (63.951°N, 21.689°W, 8.9 km); latitude and longitude have uncertainties of 0.004° and 0.008°, respectively. The hypocentre depth uncertainty is 1.3 km, allowing us to consider the possibility of a focal depth up to 7.6 km (Vogfjörð 2003; personal communication 2003). The Hvalhnúkur fault is assumed here as a north–south, vertical, right-lateral fault as, in AEA06 and Árnadóttir *et al.* (2004).

The main goals of this paper can be summarized as follows.

- (i) To study the instantaneous remote triggering of one of the early events of the 2000 June seismic sequence in SISZ by means of a realistic 3-D fault model, including heterogeneities in the crustal profile and in the fault rheology.
- (ii) To characterize the initial stress on the fault of the early event studied here, by comparing the available observations with the 3-D model estimates of hypocentre location, rupture extension and seismic moment, as well as the model failure time. In the light of this fact, we extend the conclusions of AEA06.
- (iii) To study the dependence of the response of the triggered fault on the assumed constitutive relation: rate- and state-dependent laws and slip-dependent law.

2 THE NUMERICAL APPROACH

2.1 Basic ingredients

First of all, we compute the stress field variations due to the June 17 main shock using the discrete wavenumber and reflectivity code developed by Cotton and Coutant (1997) and assuming exactly the same set of parameters and the same ramp source time function

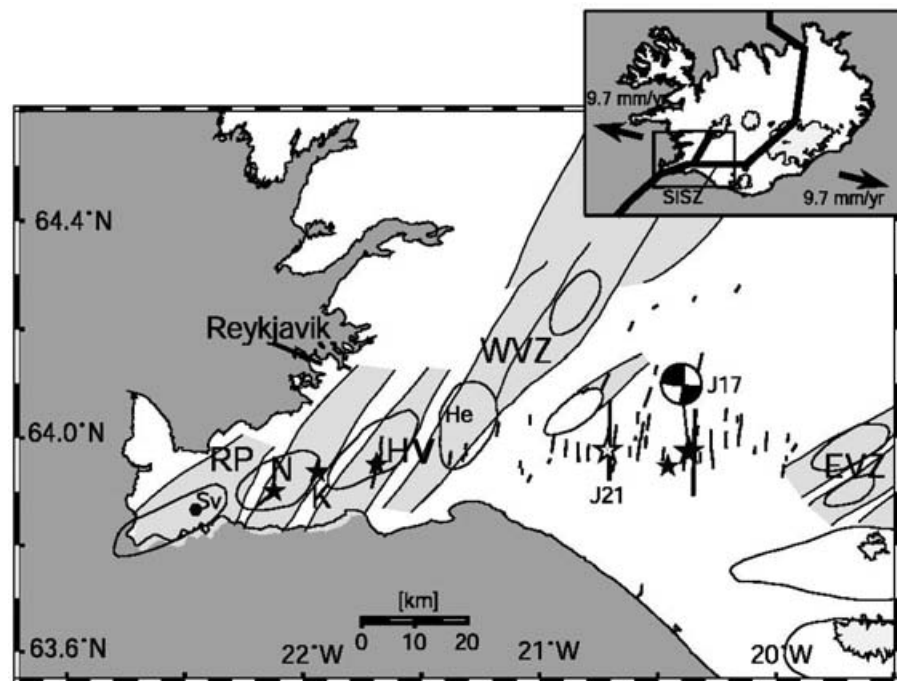


Figure 1. Location of the two main shocks (large stars) of 2000 June 17 (J17) and 2000 June 21 (J21) and aftershocks occurring within five minutes after the first main shock (small stars) in the South Iceland Seismic Zone (SISZ). The 26 and 30 s events occurred in the Reykjanes Peninsula (RP) on the Hvalhnúkur fault (HV) and Kleifarvatn fault (K), respectively. The epicentre of the 8 s event is represented by the small black star near the J17 fault. N represents the hypocentre of the aftershock that occurred near Núpshlíðarháls nearly 5 min after the main shock. Light shaded areas are individual spreading segments with associated central volcanoes (He is the Hengill Volcano and Sv the geothermal area of Svartsengi). The Western Volcanic Zone (WVZ) and the Eastern Volcanic Zone (EVZ) are also indicated. After Árnadóttir *et al.* (2004).

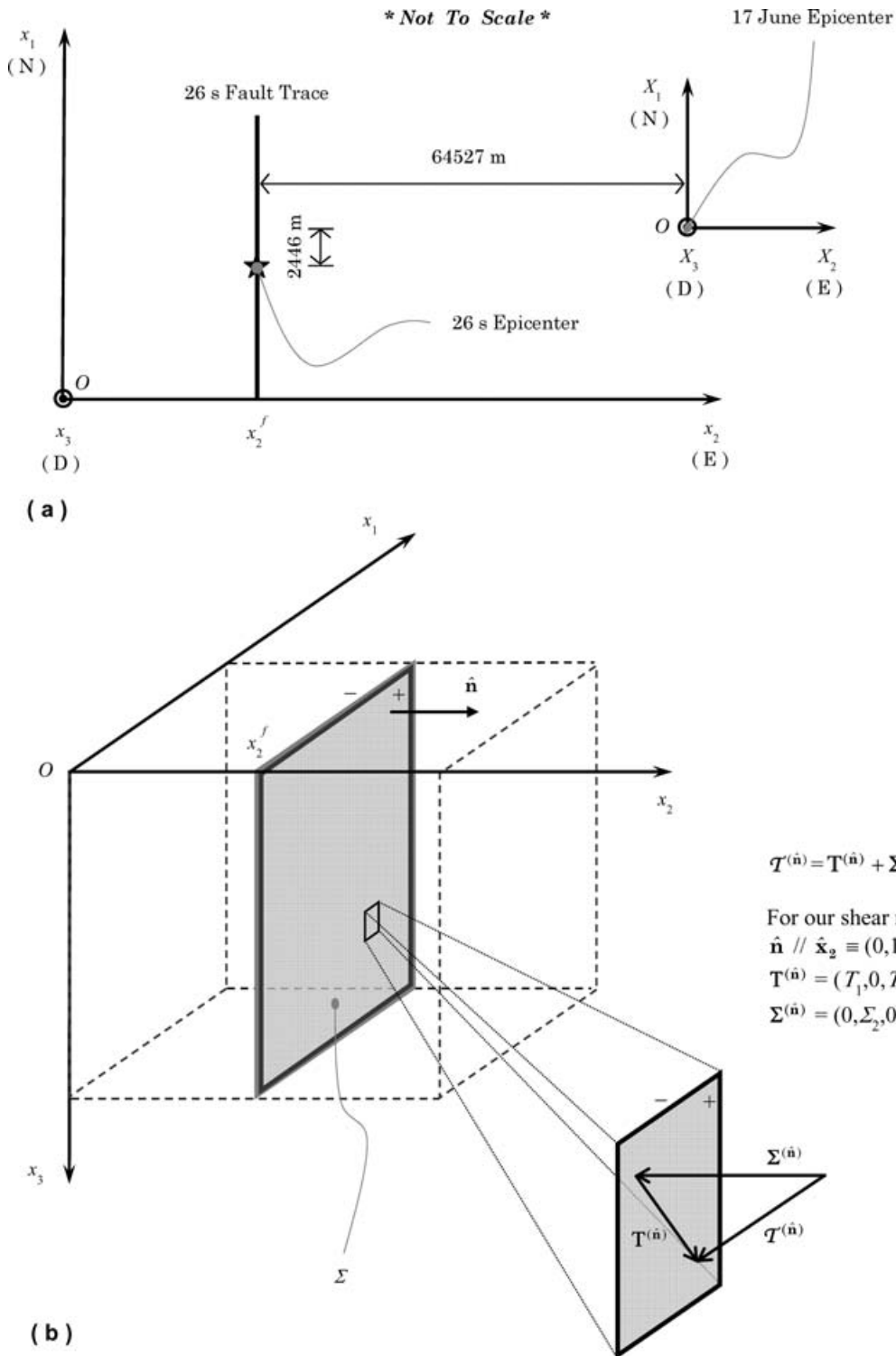


Figure 2. (a) Coordinate systems used in this work: $Ox_1x_2x_3$ is the northeast-depth system with respect to which coordinates of the receivers are defined, whereas $Ox_1x_2x_3$ is the local system. (b) Three-dimensional view of the local coordinate system—the vertical plane $x_2 = x_2^f$ (Σ) represents the fault, whereas dashed lines represent the ends of the computational spatial domain $\Omega^{(FD)}$. Considering the spatial distribution of the change of the Coulomb Failure Function in the RP (see Fig. 3 of AEA06) we have set the origin O of the $Ox_1x_2x_3$ reference frame to have the epicentre of the 26 s event located at 16.5 km in the strike direction. $\mathbf{T}(\hat{n})$ is the total traction acting on Σ ; $\mathbf{T}(\hat{n})$ is its shear component and $\Sigma(\hat{n})$ is the normal component.

$(f(t) = \frac{1}{2}[1 + \tanh(\frac{t}{t_0})])$; Bouchon 1981, with $t_0 = 1.6$ s) used in AEA06. We neglected the stress perturbations due to the 8 s aftershock owing to the large spatial distance from the 26 s event (see Fig. 1) and the smaller magnitude with respect to the main

shock. The crustal profile corresponds to the east of Hengill structure (continuous line in Fig. 2 of AEA06; see also Vogfjörð *et al.* 2002). The values of the perturbation stress tensor are calculated on the Hvalhnúkur fault plane up to 2.78 Hz, in a total of 12×8 ‘receivers’,

located in nodes uniformly spaced 1650 m in the strike direction and at depths of 0, 1650, 3300, 4950, 6550, 8100, 9900 and 11550 m. The coordinates of the receivers are expressed in a Cartesian coordinate system $OX_1X_2X_3$, having the origin O on the free surface at the epicentre of the June 17 main shock (see Fig. 2a). In the local coordinate system $Ox_1x_2x_3$, the plane Σ (Fig. 2b), defined by $x_2 = x_2^f = 5$ km, represents the 26 s fault and the nominal location of its hypocentre is (16.5, 5.0, 8.9) km.

The computed values of the stress perturbations are interpolated in space and also in time to correctly resolve the dynamic processes occurring on the Hvalhnúkur fault, according to the findings of Bizzarri & Cocco (2003, 2005) (hereafter BC05). In the following, we will indicate with $\Delta\sigma_{2i}(x_1, x_3, t)$, or more briefly with $\Delta\sigma_{2i}$ ($i = 1, 2, 3$), the results of this spatio-temporal interpolation, which is described in Appendix A.

Finally, these interpolated perturbations are included in the equations of motion representing the fully dynamic, spontaneous (i.e. without prior imposed rupture velocity) rupture problem, solved by using the *truly* 3-D (i.e. not mixed-mode) finite difference code presented in BC05 (details are summarized in Appendix B).

2.2 The response of the extended fault

In the following of the paper, a fault point is considered to fail if the modulus of its slip velocity vector, $v \equiv \sqrt{v_1^2 + v_3^2}$, is greater than or equal to a threshold value v_l , assumed to be equal to 0.1 ms^{-1} , in agreement with Belardinelli *et al.* (2003), Rubin and Ampuero (2005) and AEA06. The instant of time at which this occurs is denoted by the symbol t_p , the perturbed rupture (or failure) time. The first fault point where the condition $v \geq v_l$ is satisfied [i.e. where the minimum non-zero value of the array $t_p(x_1, x_3)$ is realized] defines what we call ‘virtual’ hypocentre (indicated with the symbol H henceforth); the adjective is motivated by the fact that this point is obtained as a part of the numerical solution. Accordingly, the least value of the perturbed failure time represents the estimate of

the origin time of the triggered event provided by this model of an extended fault.

We would emphasize that this model of an extended fault provides several additional details of the triggered event with respect to a SS analogue model of fault. In AEA06, due to the point-like approximation in the modelling of triggering, only the perturbed failure time in the observed hypocentre was given. Here we can estimate the rupture history and the slip distribution on the whole fault of the triggered event. On the other hand, this model requires a more complex parametrization of the fault surface state than SS model. The former is built upon a physical model of pore fluid pressure suitable for the SISZ and upon the comparison of synthetic solutions and other observational constraints on the extended rupture of the triggered event, reported in Appendix C.

3 RESULTS WITH THE DIETERICH–RUINA LAW

Among the different possibilities proposed in tribology (see for instance Ohnaka 2003; Bizzarri & Cocco 2005, 2006c), we assume for now that the Hvalhnúkur fault is governed by the Dieterich–Ruina (hereafter DR) rate- and state-dependent law (Linker & Dieterich 1992; AEA06; Bizzarri & Cocco 2006a, b), which expresses the frictional resistance τ as a function of the slip velocity v and the state variable Ψ (accounting for previous slip episodes) according to the following set of equations

$$\tau = \mu(v, \Psi)\sigma_n^{\text{eff}} = \left[\mu_* + a \ln\left(\frac{v}{v_*}\right) + b \ln\left(\frac{\Psi v_*}{L}\right) \right] \sigma_n^{\text{eff}},$$

$$\frac{d}{dt}\Psi = 1 - \frac{\Psi v}{L} - \left(\frac{\alpha_{LD}\Psi}{b\sigma_n^{\text{eff}}} \right) \frac{d}{dt}\sigma_n^{\text{eff}}. \quad (1)$$

In eq. (1), μ is the friction coefficient, μ_* and v_* are reference parameters; a , b and α_{LD} are the constitutive parameters, L is a scale length and σ_n^{eff} is the effective normal stress expressed by (B.3).

Table 1. Model discretization and constitutive parameters.

Parameter	Value
$\Omega^{(\text{FD})}$	Box that extends up to $x_{1\text{end}} = 36.5$ km along x_1 , up to $x_{2\text{end}} = 10$ km along x_2 and up to $x_{3\text{end}} = 11.6$ km along x_3 ^a
Σ	$\{x x_2 = x_2^f = 5 \text{ km}\}$
$\Delta x_1 = \Delta x_2 = \Delta x_3 \equiv \Delta x$	100 m ^b
Number of nodes in $\Omega^{(\text{FD})}$	4289571
Δt	$1.27 \times 10^{-3} \text{ s}^b$
Number of time levels	33650
v_l	0.1 ms^{-1}
$\varphi(x_1, x_3, 0)$	$\varphi_0 = 180^\circ$
$v(x_1, x_3, 0)$	$v_{\text{init}} = 6.34 \times 10^{-10} \text{ ms}^{-1}$ ($\approx 20 \text{ mmyr}^{-1}$)
$\Psi(x_1, x_3, 0)$	$\Psi^{\text{ss}}(v_{\text{init}}) = 1.577 \times 10^6 \text{ s}$ ($\approx 18.25 \text{ d}$)
$\sigma_n^{\text{eff}*}$	2.5 MPa
a	0.003 ^c
b	0.010
L	$1 \times 10^{-3} \text{ m}$
μ_*	0.7
v_*	v_{init}
α_{LD}	0 ^d

^aThe boundaries of $\Omega^{(\text{FD})}$ are chosen such that radiation reflected by, or interacting with, the domain boundaries largely does not affect our results in the time window here considered.

^bSee Appendix A for details about the spatio-temporal discretization.

^cIn numerical experiments with heterogeneous rheology (see Section 3.3) this is the value in the region $9700 \text{ m} \leq x_1 \leq 16500 \text{ m}$.

^dWe set $\alpha_{LD} = 0$ because including the dependence on effective normal stress in the evolution equation for the state variable has a negligible effect in cases of instantaneous triggering, unlike cases of delayed triggering (see AEA06 for a discussion). In this way, the temporal variations of the effective normal stress influence the fault traction only through the explicit dependence of τ on σ_n^{eff} .

Table 2. Synoptic list of the selected ensemble of numerical models discussed in this paper. DR stands for Dieterich–Ruina governing law (eq. 1), RD for Ruina–Dieterich (eq. 2) and OY for Ohnaka–Yamashita slip-weakening (eq. 3). The initial effective normal stress is assumed to vary with depth as for profile number 3 in Fig. 4(b), unless otherwise specified.

Case	Constitutive law	Heterogeneous rheology	Hypocentre location ^a (km)	Origin time ^a (s)	Total seismic moment M_0 (Nm)	Figures
A ^b	DR	No	(16.5, 2.9)	23.47	2.23×10^{19}	3
B	DR	No	(13.2, 7.5)	24.94	6.43×10^{16}	5, 7
C	DR	Yes	(13.2, 7.5)	24.94	2.27×10^{16}	6
D	RD	Yes	(15.7, 7.9)	23.44	2.02×10^{16}	8
E	OY	No	(22.5, 7.7)	23.70	2.49×10^{19}	9
F ^c	DR	No	(13.2, 7.5)	26.42	5.25×10^{16}	10
Observational constraints			(16.5 \pm 0.45, 8.9 \pm 1.3)	25.9 \pm 0.1	[3.2 $\times 10^{16}$, 1.8 $\times 10^{17}$]	N/A

^aIn case of model results, we indicate as hypocentre the ‘virtual’ hypocentre H and as origin time the least perturbed failure time (see Section 2.2). All times are referred to the 2000 June 17 mainshock origin time.

^bIn this case: $\sigma_n^{\text{eff}} = \sigma_n^{\text{eff}*}$.

^cThe source time function is a translated form of the original ramp function (see Section 7 for details), having the same characteristic time.

The values of the constitutive parameters used in this paper, if not otherwise mentioned, are listed in Table 1. In all cases presented in Sections 3–5 we assume, as in AEA06, that at $t = 0$ the fault is in steady state conditions, that is, $(d/dt)\Psi = 0$ in eq. (1).

3.1 A simple test case

To explain remote instantaneous triggering on the Hvalhnúkur fault with the DR law, one of the conclusions of AEA06 was that the parameter $A = a\sigma_n^{\text{eff}}$, characterizing the direct effect on friction, has to be small enough. Consequently, due to the possible values of a , a very small value of the effective normal stress (or equivalently a near-lithostatic pore fluid pressure) at the hypocentral depth of the triggered event is required.

We first verified that if pore fluid pressure is hydrostatic at every depth, no triggering occurs in this extended fault model. In a subsequent test case (case A in Table 2), we chose the most simple configuration (even if physically unrealistic), in which the initial effective normal stress is everywhere equal to $\sigma_n^{\text{eff}*} = 2.5$ MPa, as estimated by AEA06 in the hypocentre of the studied event. The resulting rupture times are reported in Fig. 3 from which we can see that the model rupture reaches the surface in contradiction of the

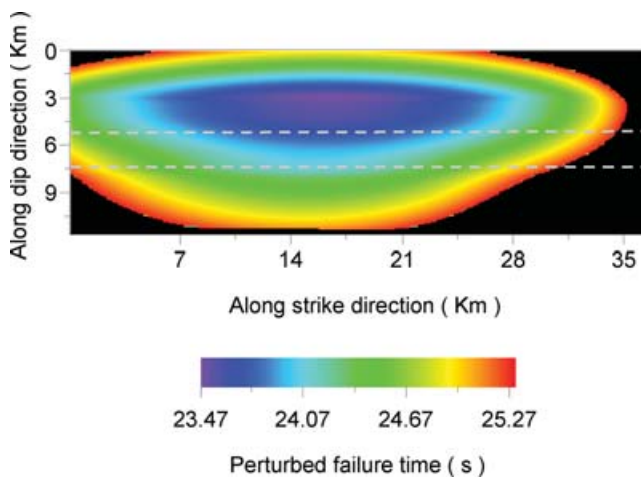


Figure 3. Distribution of the perturbed rupture times obtained for the test case A in Table 2. All model parameters are listed in Table 1, the initial effective normal stress is homogeneous on the whole fault plane and equal to 2.5 MPa and the Dieterich–Ruina governing law [eq. (1)] is assumed. The black regions indicate where $v < v_l$. The two dashed grey lines identify the area \mathcal{I} that is expected to behave seismically (see Appendix Section C.1).

observational constraints (Appendix C.1). In fact, the magnitude of the event, the depth of the hypocentre, the absence of geodetic co-seismic signals and surface effects (Clifton *et al.* 2003; Árnadóttir *et al.* 2004) and the aftershock distribution (Hjaltadóttir & Vogfjörð 2005) suggest that the seismic rupture of the induced event is confined below several kilometre depth. From Table 2 we can see that in case A, the vertical extent of the rupture area is overestimated as well as the seismic moment, which is calculated as explained in Appendix C.1. In the following of the paper, we will therefore illustrate other test cases performed to find whether it is possible to better reproduce observations by assuming a more realistic initial effective normal stress profile.

3.2 Experiments with spatially variable initial normal stress

We introduce an initial effective normal stress (σ_n^{eff}) that varies with depth, as physically reasonable for the seismogenic region considered here (Zencher *et al.* 2006). The pore fluid pressure is assumed to be hydrostatic below the depth $x_3^* = 5800$ m, and near-lithostatic for $x_3 \geq x_3^* + D^* = 8800$ m (Fig. 4a). The choice of these depth values delimiting the so-called transition region is discussed and justified in Appendix Section C.2.

A first attempt to model σ_n^{eff} is profile number 1 (dashed grey line in Fig. 4b), where we assume a near-lithostatic pore pressure for $x_3 > x_3^*$ (dashed grey line in Fig. 4a). With this profile, we inhibit the rupture propagation at shallow depth ($x_3 < x_3^*$). This is a consequence of the increase of σ_n^{eff} with decreasing depth, which in turn causes the parameter A to increase. However, with profile number 1, we overestimate the total seismic moment ($M_0 = 1.94 \times 10^{17}$ N m). A second attempt is represented by profile number 2 (dotted grey line in Fig. 4b) where the increase from hydrostatic to near-lithostatic pore pressure values is linear within the transition region (dotted grey line in Fig. 4a), as corroborated by the model of Zencher *et al.* (2006). In this case, we cannot obtain nucleation at all, since the threshold value v_1 is never attained on the fault.

Finally we consider profile number 3 (continuous grey line in Fig. 4b), in which the effective normal stress is intermediate between profile number 1 and 2 near the top of the transition region, within a depth range of a limited extension h^* ($h^* < D^*$), below which it is closer to profile number 2. Profile number 3 is expressed by eq. (C.2) in Appendix C. The pore pressure generating profile number 3 tends more rapidly than profile number 2 to near-lithostatic values with increasing depth in the transition region (continuous grey line in Fig. 4a). The results obtained with this profile for $h^* = 360$ m are reported in Fig. 5 (case B in Table 2). The least

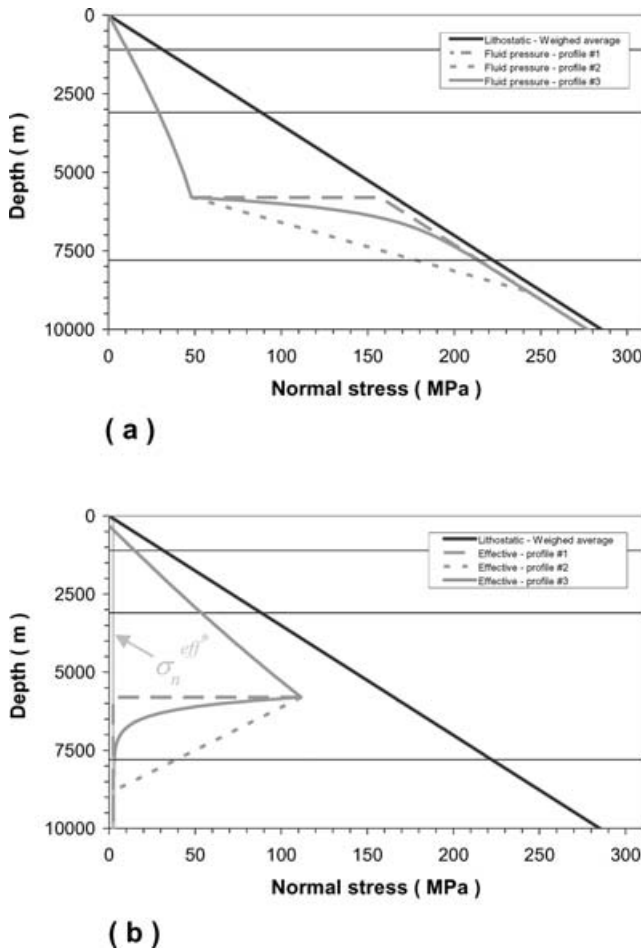


Figure 4. (a) Initial pore fluid pressure profiles considered in this study. (b) Initial effective normal stress profiles corresponding to the three profiles of p_{fluid} displayed in panel (a). The solid grey line corresponds to eq. (C.2), with $x_3^* = 5800$ m, $D^* = 3000$ m and $h^* = 360$ m. The reference initial effective normal stress $\sigma_n^{\text{eff}*}$ (vertical thin grey line) is superimposed for comparison (in case A, we assume $\sigma_n^{\text{eff}} = \sigma_n^{\text{eff}*}$ as a constant with depth).

value of the perturbed failure time is slightly lower than the observed origin time; however, as a consequence of the hydrostatic pore fluid pressure values at shallow depth, the vertical rupture extension now agrees with observations—it does not propagate above a depth of 6400 m, which is one kilometre below the limit inferred from aftershocks distributions (see Appendix Section C.1). By comparison with case A, in case B we may observe that the increase of the frictional resistance for decreasing depths is able to limit the rupture in the strike direction too. For this synthetic event, the total seismic moment estimate is $M_0 = 6.43 \times 10^{16}$ Nm, which corresponds to a moment magnitude $M_w = 5.21$, in the range of observations. The underestimates of the observed origin time obtained here can be related to the source time function used in AEA06, as we will discuss in detail in Section 7.

Looking at the time snapshots of the slip velocity on the fault plane (Figs 5b–d), we can see a pulse propagating towards the free surface and expanding in the strike direction. Below the depth of 7500 m, the fault-slip velocity remains well below v_l .

3.3 Heterogeneous rheology

To reproduce the confinement of the triggered rupture along the strike direction that can be roughly envisaged by the aftershock

distribution (region A defined in Appendix Section C.1), we have assumed a velocity strengthening rheology (i.e. $a > b$; $a = 0.012$) for $x_1 < 9700$ m and $x_1 > 16500$ m. These regions are associated with aseismic behaviour and they act like barriers (see Bizzarri *et al.* 2001).

The resulting rupture times of this case C are shown in Fig. 6 (see also Table 2). The coordinates of H, its failure time and the extension along the dip of the rupture are identical to those obtained in the previous, fully homogeneous case B, that is, the fault evolution in H is practically unaffected by the presence of the lateral velocity strengthening areas. However, now the seismic rupture is confined in the velocity weakening region $9700 \text{ m} \leq x_1 \leq 16500 \text{ m}$, as expected by the imposition of artificial barriers. Consequently, the seismic moment is now $M_0 = 2.27 \times 10^{16}$ N m ($M_w = 4.90$), which is smaller than the lower bound of the acceptable range (see Appendix Section C.1). All this information tends to suggest that the *ad hoc*-imposed lateral rheological heterogeneities do not significantly improve the results of numerical model.

4 COMPARISON WITH SPRING-SLIDER RESULTS

In this section, we focus our attention on the temporal evolution of dynamic variables in the location of H for the previously discussed case B. In Fig. 7, results of this extended fault (3-D model; black solid squares) are compared with those obtained with a SS analogue model (grey open circles). In the SS numerical experiment, we introduce the same stress perturbations acting in the target point of the 3-D simulation. The comparison is made assuming the same constitutive parameters and governing law.

Looking at Fig. 7(a), we can see that the solutions of the 3-D and SS fault models agree in the first part of the simulation, for very low values of slip velocity. This confirms that the quasi-static approximation used in the SS simulation is adequate for low values of slip velocity. We emphasize again that in all 3-D numerical experiments presented in this paper, the system is fully dynamic in the whole range of variability of fault-slip velocity. The agreement between the two solutions is good until the time $t_A = 24.10$ s (light grey dashed line in Figs 7a, b and d), corresponding to the largest peak of the shear stress perturbation ($-\Delta\sigma_{21}$ in notation) and to the beginning of the acceleration phase in the 3-D model (Fig. 7b). For $t > t_A$, the two solutions become different—the 3-D system accelerates up to final instability ($t_p = 24.94$ s, full vertical line in Figs 7a, b and d) whereas in the SS model, the slip velocity remains smaller than v_l and, after a deceleration phase (ending in the point B in Fig. 7a), it slowly increases again with time to provide a delayed failure of the system at $t = 3.36$ d (not shown in Fig. 7).

This different behaviour of the two models can be explained considering the different elastic loads exerted on the two systems. Unlike the SS, the 3-D model in H is also affected by the load \mathbf{f}_r exerted by the neighbouring points that, even moving with $v < v_l$, produce shear and normal loads that at each time level are superimposed on the stress perturbations due to June 17 main shock (see Appendix B). This contribution in the strike component of total shear load is clearly visible in Fig. 7(d), where we can see that for $t < t_A$, the shear loads are indistinguishable in the two models; but just before the peak of the shear stress perturbation, the load \mathbf{f}_r begin to become significant, increasing the peak of the total shear load in the 3-D model (reached at $t = 24.30$ s $> t_A$). This peak is high enough to enhance seismic slipping in the 3-D model, unlike the SS model.

From the slip-weakening curve (Fig. 7c), we can see that the maximum value of traction (τ_u^{eq}) is the same in both models, as well

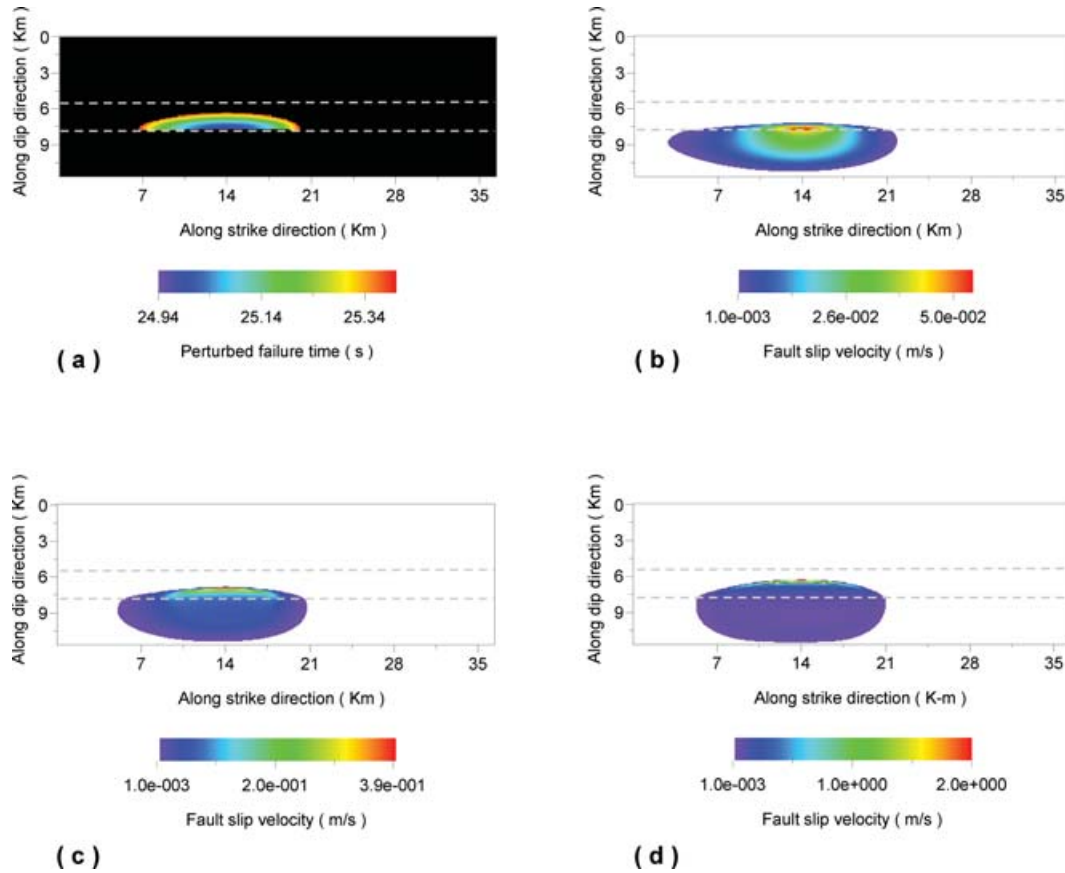


Figure 5. (a) The same as in Fig. 3, but now (case B in Table 2) the initial effective normal stress is variable along the depth as in profile number 3 shown in Fig. 4(b) (solid grey line). Snapshots of the fault-slip velocity just before the triggered instability ($t = 24.76$ s; panel b) and after t_p , at $t = 25.08$ s (panel c) and at $t = 25.40$ s (panel d). In all panels the dashed grey lines identify the area I that is expected to behave seismically (see Appendix Section C.1).

as the final or level of traction (τ_f^{eq}), that is, the kinetic frictional resistance and the equivalent slip-weakening distance (d_0^{eq}). The latter represents the amount of fault-slip over which the traction decreases from its maximum value down to the residual kinetic level (Cocco & Bizzarri 2002; Bizzarri & Cocco 2003). The two curves differ for slip values smaller than the value reached at point C in Fig. 7(c). Actually, in the SS case there is an early partial stress release (first weakening episode) that occurs at $t \cong t_A$ when the first peak of slip velocity is realized (Fig. 7a).

In this study, as in the 2-D study made by Bizzarri & Cocco (2003), we can note that the failing point accelerates and exceeds the threshold velocity $v_l = 0.1 \text{ m s}^{-1}$ (i.e. it behaves seismically—grey star in Fig. 7d) before the traction reaches its kinetic level, unlike what was stated by Voisin *et al.* (2004). This is even more evident if we decrease the threshold value of sliding velocity—with $v_l = 0.05 \text{ m s}^{-1}$ the failure point fails in the middle of weakening process and with $v_l = 0.01 \text{ m s}^{-1}$ it is just at the beginning of the breakdown phase (open black stars in Fig. 7c).

5 IMPORTANCE OF THE GOVERNING LAW: THE RUINA-DIETERICH MODEL

In this section we assume a different evolution equation for the state variable, the so-called slip law (Ruina 1983) to quantify how results are affected by this different governing law. In this constitutive model—referred as RD thereafter—the frictional traction can be

written as (Beeler *et al.* 1994; Bizzarri & Cocco 2006a, b):

$$\tau = \left[\mu_* + a \ln \left(\frac{v}{v_*} \right) + b \ln \left(\frac{\Psi v_*}{L} \right) \right] \sigma_n^{\text{eff}}, \quad (2)$$

$$\frac{d}{dt} \Psi = -\frac{\Psi v}{L} \ln \left(\frac{\Psi v}{L} \right) - \left(\frac{\alpha_{LD} \Psi}{b \sigma_n^{\text{eff}}} \right) \frac{d}{dt} \sigma_n^{\text{eff}}.$$

We adopt the same governing parameters used in simulations presented in Sections 3.2 and 3.3 (cases B and C) and therefore the initial conditions are also the same. However, due to the different evolution of Ψ , for $t > 0$ the values of the frictional traction τ are different.

Results for this configuration (case D) are shown in Fig. 8. The rupture has nearly the same extension along strike as in case C, because it has been obtained using the same velocity strengthening regions as rheological barriers. In spite of this, compared to case C, the vertical extension of the rupture is larger and the seismic moment $M_0 = 2.02 \times 10^{16} \text{ Nm}$ ($M_w = 4.87$) is smaller, suggesting that the RD law predicts a slightly smaller average fault slip than the DR law.

In this case we obtain the smallest perturbed failure time, $t_p = 23.44$ s (black continuous lines in Figs 8b and c). Perturbed failure occurs before the time of the peak of the along strike component of the stress perturbation (now $t_A = 24.03$ s; light grey dashed lines in Figs 8b and c). Accordingly, the time delay $t_d = t_p - t_A$ is negative, $t_d = -0.59$ s (Fig. 8c). These differences can be explained recalling that the RD law is more unstable than the DR law for the same initial conditions and constitutive parameters (e.g. Belardinelli

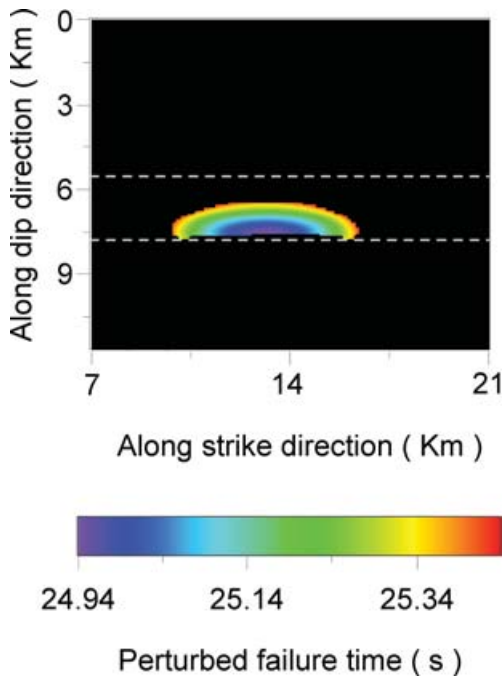


Figure 6. Perturbed failure times for the case C in Table 2—parameters are the same as for Fig. 5, but now the parameter a is equal to 0.012 for $x_1 < 9700$ m and $x_1 > 16500$ m. Note that to emphasize the cracked area we report only a portion of the whole fault plane.

et al. 2003; Bizzarri & Cocco 2003). The traction versus slip curve (Fig. 8d) shows an equivalent slip-weakening distance nearly 5 mm long: it is therefore smaller than that arising from the DR law, in agreement with Bizzarri & Cocco (2003). Finally, we remark that in the case of RD law also, H accelerates to instability before reaching the final kinetic frictional level (grey star in Fig. 8d).

With the RD law we perform the same comparison between the 3-D model and the SS model made in the previous section. Unlike the previous results, using the RD law, the SS model also shows instantaneous dynamic triggering. Both the SS and the 3-D models are characterized by negative time delays (see Fig. 8c), but the perturbed failure time in the SS model is $t_p = 23.93$ s, larger than in the 3-D model. We can therefore exclude the possibility of estimating a larger value of origin time of the triggered event by using a more complex and realistic model of fault, such as the 3-D model, in place of a SS model, for the same governing law, constitutive parameters, initial conditions and perturbing stress. Moreover, it is confirmed that the 3-D model is more unstable than the SS model, due to the different elastic loads, as discussed in the previous section.

6 THE NON-LINEAR SLIP-WEAKENING FRICTION LAW

One alternative to the class of rate- and state-dependent governing equations is represented by the slip-dependent laws; here we have considered the following non-linear form of the slip-weakening (see for instance, Ohnaka & Yamashita 1989):

$$\tau = \left\{ \left[\left(\frac{\tau_0}{\sigma_n^{\text{eff}}} - \mu_f \right) \left(1 + \alpha_{\text{OY}} \ln \left(1 + \frac{u}{\beta_{\text{OY}}} \right) \right) \right] e^{-\frac{u}{d_0}} + \mu_f \right\} \sigma_n^{\text{eff}}, \quad (3)$$

where α_{OY} and β_{OY} are constitutive parameters that control the slip-hardening phase, μ_f is the dynamic (or kinetic) value of the

friction coefficient and u is the fault slip. The coupling of fault strength with stress perturbations is again expressed by eqs (B.1) and (B.2).

As explained in Appendix D, the governing parameters in eq. (3) are chosen to reproduce the slip-weakening curve previously obtained with DR law (Fig. 7c). In this configuration (case E), H is located at (22500, 7700) m (see Fig. 9a), far from the strike location of the observed hypocentre, and the estimate of the seismic moment is $M_0 = 2.49 \times 10^{19}$ N m, much larger than the maximum value suggested by observations. In this case, unlike case B, the initial effective normal stress is actually unable to confine the rupture within the depth interval \mathcal{I} suggested by observations (see Appendix C.1), and a slip velocity of several metres per second is attained, even at the free surface (see Fig. 9b). On the other hand, imposing a confinement of the rupture by introducing frictional heterogeneities (formally we set a sufficiently high fault strength for $x_1 < 9700$ m and $x_1 > 16500$ m and for $x_3 > x_3^* + D^*$), the threshold value v_f is never attained on the fault.

In principle, we can not exclude that for a specific set of constitutive parameters appearing in eq. (3), the fault strength is such that nucleation will be confined at depth in agreement with the observations, but such a systematic exploration of the parameter domain is certainly beyond the objectives of this work. We only note that, unlike the rate- and state-dependent laws, for a set of constitutive parameters giving the same frictional resistance, the non-linear slip-weakening law (even with its initial slip-hardening phase mimicking the direct effect of rate- and state-dependent laws) is not able to reproduce the main physical features of the aftershock considered in this paper.

7 DISCUSSION AND CONCLUSIONS

In this paper, we present results of numerical experiments of a *truly* 3-D fault model where the external perturbations of fault traction due to a remote earthquake are taken into account, and both components of fault-slip and slip velocity (and then rake rotation) are found from one vectorial constitutive relationship, unlike mixed-mode fault models. Moreover, different constitutive laws are considered here for the fault rheology. We focus our attention on the ‘instantaneous’ dynamic triggering phenomenon (triggering realized after the arrival of the seismic waves propagating from the causative event with a delay smaller than the wave train duration). This effect, also called ‘immediate’ or ‘with no delay’, can explain early events occurring after a main shock (at times, of the order of the traveltime of the seismic wave generated by the main shock). Transient stress perturbations, such as seismic waves at remote distance, can induce mainly this kind of short-term triggering effects according to several models where failure is assumed to be preceded by an accelerating phase (e.g. Gombert 2001; Belardinelli *et al.* 2003). The observational evidence of early events is scarce compared with delayed aftershocks that are, instead, widely observed during a seismic sequence (e.g. Ziv 2006). This can be due to the intrinsic difficulty to detect a seismic event occurring within the wave train packet generated by a previous event and the peculiarity of regions where these effects were observed and interpreted, mainly volcanic or geothermal provinces.

Using the rate- and state-dependent laws and a SS model of fault, instantaneous dynamic triggering can be reproduced provided that the perturbed fault is in critical conditions (e.g. Belardinelli *et al.* 2003), that is, assuming fine tuned values of the model parameters. One of the main motivations of this paper is to see if it is possible

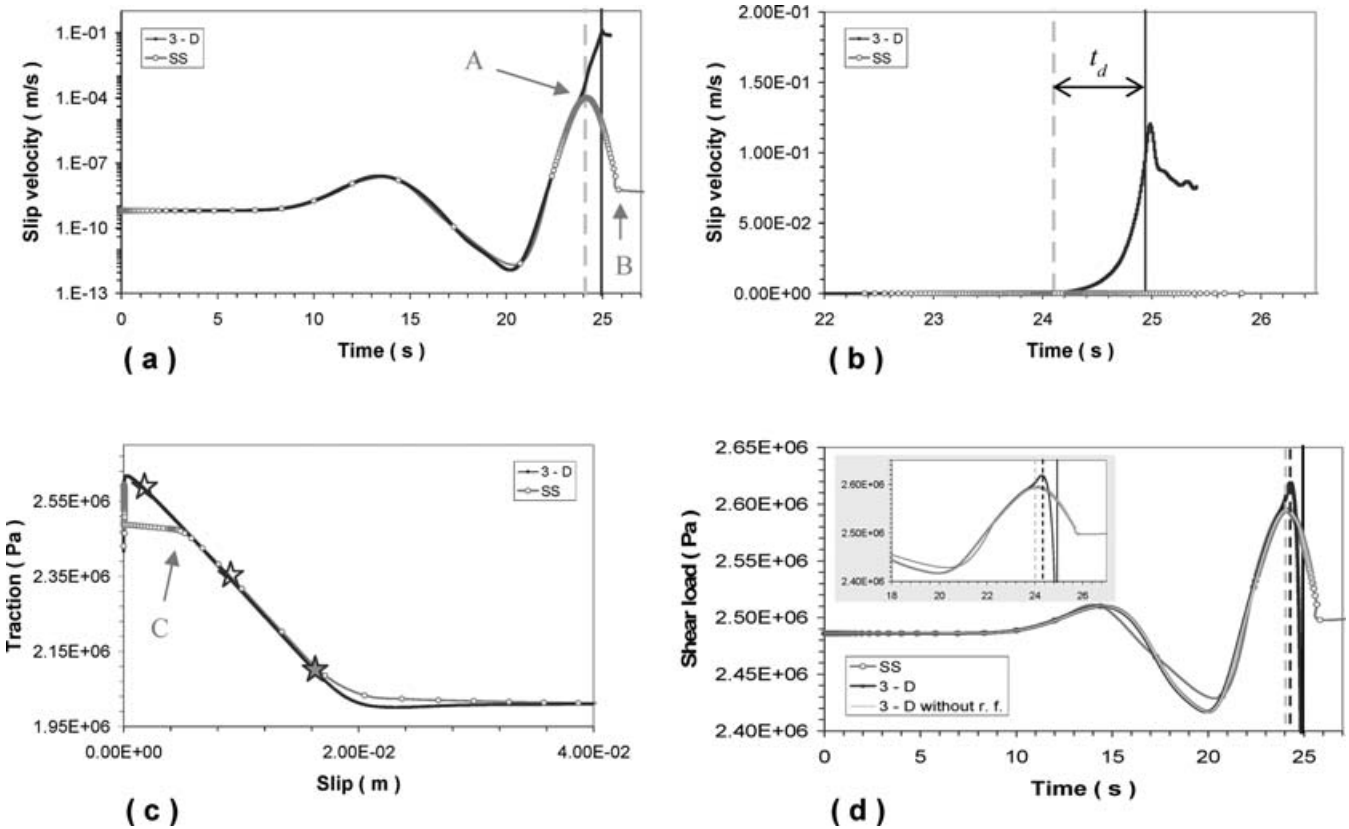


Figure 7. Comparison of the solutions in H from the 3-D fault model corresponding to Fig. 5 (black solid squares; 3-D) and a spring–slider model (grey open circles; SS). (a) Fault-slip velocity-time history. (b) Particular of the fault-slip velocity time history in a shorter time window. (c) Slip-weakening curve; the grey star denotes the state of the system when $v = 0.1 \text{ m s}^{-1}$ (at $t = t_p$) whereas the two black open stars denote the points at which v is 0.01 and 0.05 m s^{-1} . In the two slip-weakening curves, points with the same value of slip do not correspond to the same value of time. (d) Total loads (namely $-\mathcal{L}_1^{(3-D)} = -f_{r1} + \tau_0 - \Delta\sigma_{21}$ and $\mathcal{L}^{(SS)} = \tau_0 - \Delta\sigma_{21}$; f_{r1} is the strike component of the dynamic load, see Appendix B for details). If we subtract f_{r1} from $\mathcal{L}_1^{(3-D)}$, we obtain the thin grey line, coincident with $\mathcal{L}^{(SS)}$, as expected. In panels (a), (b) and (d) vertical light grey dashed lines indicate the time of the peak in $-\Delta\sigma_{21}(t = t_A = 24.10 \text{ s})$ whereas vertical full lines denote the perturbed failure time for the 3-D model ($t_p = 24.94 \text{ s}$). The time interval between vertical full lines and vertical light grey dashed line is the time delay t_d . The black dashed line in panel (d) indicates the peak of $-\mathcal{L}_1^{(3-D)}(t = 24.30 \text{ s})$.

to reproduce this kind of triggering effects with an extended fault model and adopting different governing laws on the fault.

As an application of the model, we consider the fault interaction occurred between the 2000 June 17 mainshock in the SISZ and the early event that occurred after 26 s on the Hvalhnúkur fault, which is located at a remote distance from the main shock (about 64 km). From a seismological point of view, this event is constrained the best among the three early aftershocks observed within 30 s after the 2000 June 17 main shock. Moreover, for this event the interactions with previous seismic events other than the main shock can be reasonably excluded. We aim to remark that our model can be applied to other cases of instantaneous triggering even if, as in all computational experiments, the value of the parameters of the model have to be tuned according to the specific event we want to reproduce, assuming that enough observational knowledge of the event is available.

The fundamental elasto-dynamic equation accounting for the stress perturbations due to the main shock is solved without any approximations in the whole range of fault-slip velocity by using the finite difference code presented in BC05. Both shear and normal components of the stress perturbation tensor are accounted for (in agreement with the Coulomb failure criterion, largely used in fault interaction studies), as well as the heterogeneous properties of the elastic medium surrounding the 26 s fault. The stress perturbations

are calculated by using the discrete wavenumber and reflectivity method on the whole Hvalhnúkur fault plane.

The three early aftershocks observed in the SISZ were analysed in a previous paper (AEA06) where the conditions to reproduce the origin time of all of them were already stated by means of a spring–slider (SS) model. The results presented here are new with respect to that paper, as well as previously published studies of instantaneous dynamic triggering that used a 2-D fault model (Voisin *et al.* 2000) to describe the fault response. In fact, only by adopting a 3-D fault model it is possible to obtain, as a part of the solution, several additional and important details of the simulated triggered event, such as the rupture history on the whole fault surface and the seismic moment. These numerical estimates are compared with available observations.

Our 3-D modelling of the Hvalhnúkur fault inevitably requires a more detailed parametrization than previous modelling since the state of the fault should be specified in each point of its surface. In general, we assume the same homogeneous conditions as in AEA06, except for the initial effective normal stress σ_{n0}^{eff} for which we assume a depth dependence in agreement with an independent physical model proposed for the SISZ (Zencher *et al.* 2006) and with the value estimated by AEA06 at hypocentral depth. In the Zencher *et al.* (2006) model, an increase from hydrostatic to near-lithostatic pore fluid pressure, within the so-called transition zone, is realized

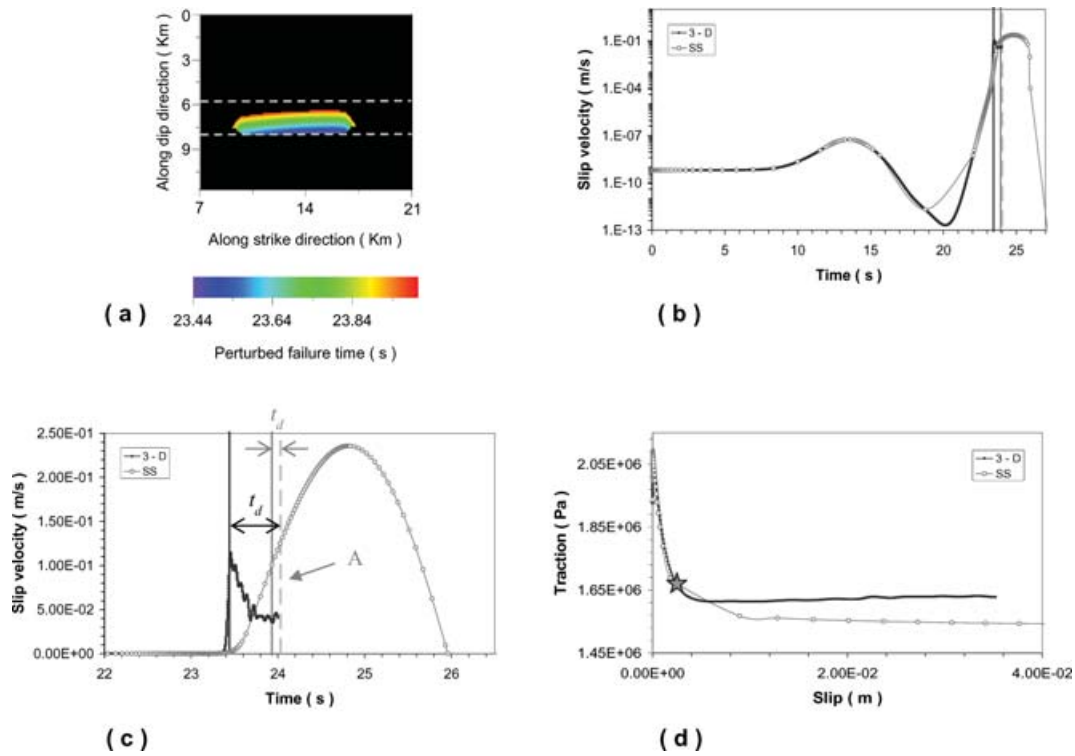


Figure 8. (a) The same as in Fig. 6(a), but in the case of Ruina–Dieterich model (eq. (2); case D in Table 2). (b) Fault-slip velocity time history in H. (c) Detail of the fault-slip velocity–time history in a shorter time window. (d) Slip-weakening curve. Black solid squares refer to the 3-D model, while grey open circles to the spring–slider model. In panels (b) and (c) vertical light grey dashed lines indicate the time of the peak of $-\Delta\sigma_{21}$ ($t = t_A = 24.03$ s) whereas vertical full lines denote the perturbed failure times ($t_p^{(3-D)} = 23.44$ s and $t_p^{(SS)} = 23.93$ s). The grey star in panel (d) denotes the point in the slip-weakening curve corresponding to the perturbed failure time.

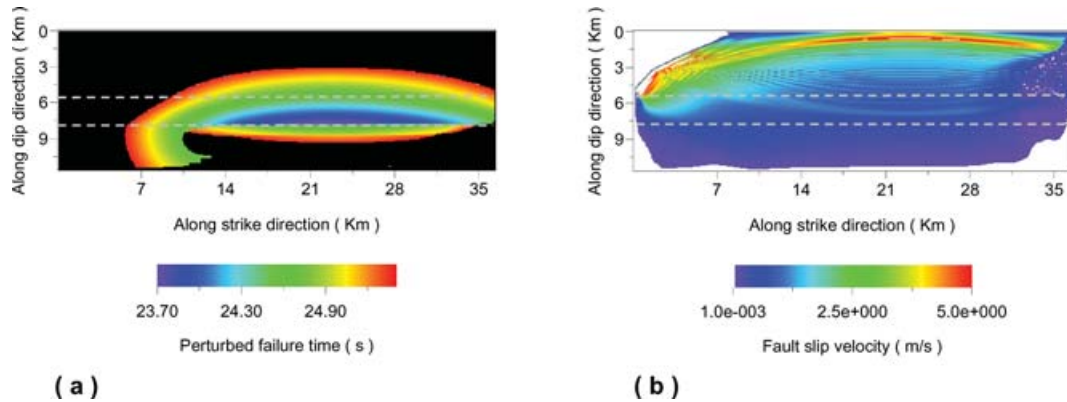


Figure 9. (a) The same as in Fig. 5(a), but assuming the non-linear slip-weakening constitutive model (eq. 3; case E in Table 2). To help the comparison, we plot rupture times up to the maximum value of Figs 5(a) and 6. (b) Time snapshot of the fault-slip velocity at $t = 27$ s.

at seismogenic depth (see Fig. 4). In the case of the early aftershock examined here, this choice was shown to be efficient in explaining the limited vertical extent of the triggered rupture suggested by several lines of evidence, avoiding the *ad hoc* introduction of other kinds of barriers.

One important result of this paper is that we can reproduce dynamic triggering effects (i.e. the induced failure) with a model of an extended fault, regardless the constitutive law. This is not a trivial result, considering the findings of Belardinelli *et al.* (2003) who thoroughly described the extreme difficulty to model dynamic triggering with the rate- and state-dependent laws. Moreover, for the 26 s early event in the SISZ, we show here that with rate- and state-dependent

laws and profile number 3 of Fig. 4, we can obtain estimates of the perturbed failure time, vertical extension of the fault rupture, hypocentre location and the seismic moment in general agreement with the available observational constraints (cases B to D).

The comparison between the two formulations of the rate- and state-dependent laws (cases C and D) confirms previous results (e.g. Belardinelli *et al.* 2003) showing that the RD law (cases D; Fig. 8) is more unstable than the DR law (case C; Fig. 6). In particular, the RD law is shown to provide the smallest perturbed failure time.

We have also compared the time evolution of solutions in the ‘virtual’ hypocentre obtained with a SS model and the present 3-D one. These two fault models are intrinsically different, but both

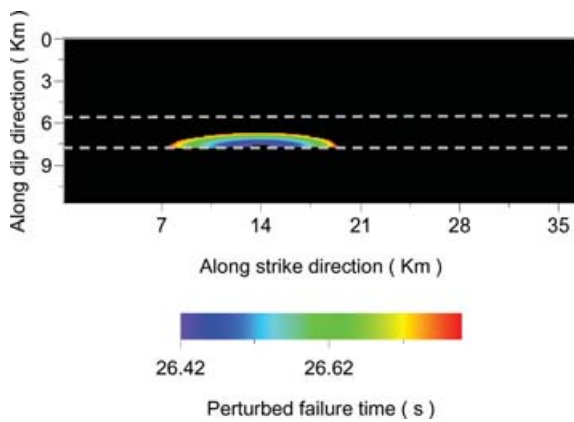


Figure 10. The same as in Fig. 5(a), but assuming a translated form of the Bouchon ramp source time function (case F in Table 2).

with the DR law (case B) and with the RD law (case D), we have observed an excellent agreement during the slow nucleation phase (when the fault-slip velocity is of the order of the initial one). During the subsequent acceleration phase, unlike the SS model, each point of the 3-D model is affected not only by the external stress perturbations due to the causative event but also by the load exerted by the neighbouring points that are already slipping. This implies that the estimate of the origin time of the triggered event provided by the 3-D model is systematically smaller than that given by the SS model.

Our results clearly show that the least value of the perturbed failure time on the Hvalhnúkur fault slightly underestimates the observed origin time of the 26 s event. An analogous underestimate was previously obtained with a SS model. This discrepancy could be attributed to problems in the estimate of the perturbing stress, related to (i) the assumed crustal profile and (ii) the assumed source time function. We analyse this second possibility by recomputing the stress perturbations induced by the June 17 main shock with a translated and more causal form of the Bouchon source time function [$f(t) = \frac{1}{2}[1 + \tanh(\frac{t-t_0}{t_0})]$; Cotton & Campillo 1994, again with $t_0 = 1.6$ s]. Applying these stress perturbations to a 3-D fault parametrized as in case B, we obtain almost the same spatial feature of the rupture (compare Figs 5a and 10), but a larger estimate of the least perturbed failure time ($t_p = 26.42$ s; case F in Table 2), which is closer to the observations.

We have also considered (case E in Table 2) a non-linear slip-dependent friction law with an initial hardening stage, as analytically postulated by Ida (1972; his fig. 1). This formulation can be regarded as an alternative to the rate- and state-laws and overcomes the non-physicality of other expressions of the slip-weakening law (Andrews 1976; Voisin 2002; Voisin *et al.* 2004) that predict that a fault point is completely locked before traction reaches the maximum yield stress. Nevertheless, by assuming governing parameters giving the same frictional resistance of the DR case, it is not possible to reproduce the 26 s aftershock rupture. In particular, the effective normal stress is not sufficient to arrest the crack propagation along depth, unlike the case of rate- and state-dependent laws.

To summarize, the study of the response of an extended 3-D fault to external stress perturbations performed here provides further support to a possible mechanism for the instantaneous dynamic triggering observed in the year 2000 in the SISZ. Our results suggest that the triggered rupture might be confined within the transition zone from near-lithostatic (at depth) to hydrostatic pore fluid pressure values, located just above the brittle–ductile transition depth.

ACKNOWLEDGMENTS

We would like to thank Maurizio Bonafede for providing us material in advance of publication and Paul Spudich for useful discussions. The editor Massimo Cocco and two anonymous reviewers are acknowledged for their comments.

REFERENCES

- Andrews, D.J., 1976. Rupture propagation with finite stress in antiplane strain, *J. geophys. Res.*, **81**(20), 3575–3582.
- Antonoli, A., Belardinelli, M.E., Bizzarri, A. & Vogfjörð, K.S., 2006. Evidence of instantaneous dynamic triggering during the seismic sequence of year 2000 in South Iceland, *J. geophys. Res.*, **111**, B03302, doi:10.1029/2005JB003935.
- Árnadóttir, T., Geirsson, H., Bergsson, B.H. & Völksen, C., 2000. The Icelandic continuous GPS network—ISGPS, March 18, 1999–February 20, 2000, Rep. VI-R00002-JA02, 36 pp., Icelandic Meteorol. Off., Reykjavík, Iceland.
- Árnadóttir, T., Geirsson, H. & Einarsson, P., 2004. Coseismic stress changes and crustal deformation on the Reykjanes Peninsula due to triggered earthquakes on 17 June 2000, *J. geophys. Res.*, **109**, doi:10.1029/2004JB003130.
- Árnadóttir, T., Hreinsdóttir, S., Gudmundsson, G., Einarsson, P., Heinert, M. & Völksen, C., 2001. Crustal deformation measured by GPS in the south Iceland seismic zone due to two large earthquakes in June 2000, *Geophys. Res. Lett.*, **28**, 4031–4033.
- Árnadóttir, T., Jiang, W., Feigl, K.L., Geirsson, H. & Sturkell, E., 2006. Kinematic models of plate boundary deformation in southwest Iceland derived from GPS observations, *J. geophys. Res.*, **111**, B07402, doi:10.1029/2005JB003907.
- Beblo, M. & Björnsson, A., 1980. A model of electrical resistivity beneath NE-Iceland, correlation with temperature, *J. Geophys.*, **47**, 184–190.
- Beeler, N.M., Tullis, T.E. & Weeks, J.D., 1994. The roles of time and displacement in the evolution effect in rock friction, *Geophys. Res. Lett.*, **21**(18), 1987–1990.
- Belardinelli, M.E., Bizzarri, A. & Cocco, M., 2003. Earthquake triggering by static and dynamic stress changes, *J. geophys. Res.*, **108**(B3), 2135, doi:10.1029/2002JB001779, ESE 1-1–1-16.
- Bizzarri, A. & Cocco, M., 2003. Slip-weakening behavior during the propagation of dynamic ruptures obeying rate- and state-dependent friction laws, *J. geophys. Res.*, **108**(B8), 2373, doi:10.1029/2002JB002198, ESE 3-1–ESE 3-21.
- Bizzarri, A. & Cocco, M., 2005. 3D dynamic simulations of spontaneous rupture propagation governed by different constitutive laws with rake rotation allowed, *Ann. Geophys.*, **48**(2), 279–299.
- Bizzarri, A. & Cocco, M., 2006a. A thermal pressurization model for the spontaneous dynamic rupture propagation on a three-dimensional fault. 1: methodological approach, *J. geophys. Res.*, **111**, B05303, doi:10.1029/2005JB003862.
- Bizzarri, A. & Cocco, M., 2006b. A thermal pressurization model for the spontaneous dynamic rupture propagation on a three-dimensional fault. 2: traction evolution and dynamic parameters, *J. geophys. Res.*, **111**, B05304, doi:10.1029/2005JB003864.
- Bizzarri, A. & Cocco, M., 2006c. Comment on “Earthquake cycles and physical modeling of the process leading up to a large earthquake”, *Earth Planets Space*, **58**, 1525–1528.
- Bizzarri, A., Cocco, M., Andrews D.J. & Boschi, E., 2001. Solving the dynamic rupture problem with different numerical approaches and constitutive laws, *Geophys. J. Int.*, **144**, 656–678.
- Boatwright, J. & Cocco, M., 1996. Frictional constraints on crustal faulting, *J. geophys. Res.*, **101**(B6), 13 895–13 909.
- Bouchon, M., 1981. A simple method to calculate Green’s function for layered media, *Bull. sesim. Soc. Am.*, **71**, 959–971.
- Brodsky, E.E., Karakostas, V. & Kanamori, H., 2000. A new observation of dynamically triggered regional seismicity: earthquakes in Greece

- following the August 1999 Izmit, Turkey earthquake, *Geophys. Res. Lett.*, **27**, 2741–2744.
- Byerlee, J., 1990. Friction, overpressure and fault normal compression, *Geophys. Res. Lett.*, **17**, 2109–2112.
- Byerlee, J., 1993. Model for episodic flow of high-pressure water in fault zones before earthquakes, *Geology*, **21**, 303–306.
- Camelbeeck T., van Eck, T., Pelzing, R., Ahorncr, L., Loohuis, J., Haak, H.W., Hoang-Trong, P. & Hollnack, D., 1994. The 1992 Roermond earthquake, the Netherlands, and its aftershocks, *Geologie en Mijnbouw*, **73**, 181–197.
- Clifton, A.E., Pagli, C., Jonsdottir, J.F., Eythorsdottir, K. & Vogfjörð, K.S., 2003. Surface effects of triggered fault slip on Reykjanes Peninsula, SW Iceland, *Tectonophysics*, **369**(3–4), 145–154.
- Cocco M. & Bizzarri, A., 2002. On the slip-weakening behavior of rate- and state-dependent constitutive laws, *Geophys. Res. Lett.*, **29**(11), 11–1–11–4.
- Cotton, F. & Campillo, M., 1994. Application of seismogram synthesis to the study of earthquake source from strong motion records, *Ann. Geophys.*, **XXXVII**(6), 1539–1564.
- Cotton, F. & Coutant, O., 1997. Dynamic stress variations due to shear faults in a plane layered medium, *Geophys. J. Int.*, **128**, 676–688.
- Crampin, S., Volti, T., Chastin, S., Gudmundsson, A. & Stefánsson, R., 2002. Indication of high pore fluid pressures in a seismically-active fault zone, *Geophys. J. Int.*, **151**, F1–F5.
- de Boor, C., 1978. *A Practical Guide to Splines*, Springer-Verlag, New York.
- De Martini, P.M., Pino, N.A., Valensise, G. & Mazza, S., 2003. Geodetic and seismologic evidence for slip variability along a blind normal fault in the Umbria-Marche 1997–1998 earthquakes (central Italy), *Geophys. J. Int.*, **155**(3), 819–829.
- Dziewonski, A.M., Chou, T.A. & Woodhouse, J.H., 1981. Determination of earthquake source parameters from waveform data for studies of global and regional seismicity, *J. geophys. Res.*, **86**, 2825–2852.
- Eberhart-Phillips, D. *et al.*, 2003. The 2002 Denali Fault Earthquake, Alaska: a large magnitude, slip-partitioned event, *Science*, **300**, 1113–1118.
- Gomberg, J., 2001. The failure of the earthquake failure models, *J. geophys. Res.*, **106**, 16 253–16 263.
- Gomberg, J., Blanpied, M.L. & Beeler, N.M., 1997. Transient triggering of near and distant earthquakes, *Bull. seism. Soc. Am.*, **87**, 294–309.
- Gomberg, J., Beeler, N.M., Blanpied, M.L. & Bodin, P., 1998. Earthquake triggering by transient and static deformations, *J. geophys. Res.*, **103**, 24 411–24 426.
- Gomberg J., Resenberg, P.A., Bodin, P. & Harris, R.A., 2001. Earthquake triggering by seismic waves following the Landers and Hector Mine earthquake, *Nature*, **411**, 462–466.
- Haar, L., Gallagher, J.S. & Kell, G.S., 1984. *NBS/NRC Steam Tables*, Hemisphere Publ. Co., NY.
- Hersir, G.P., Björnsson, A. & Pedersen, L.B., 1984. Magnetotelluric survey across the active spreading zone in southwest Iceland, *J. Volcanol. Geotherm. Res.*, **20**, 253–265.
- Hjaltadóttir, S. & Vogfjörð, K.S., 2005. Subsurface fault mapping in Southwest Iceland by relative location of aftershocks of the June 2000 earthquakes, *Report Rit Védurstofu Íslands*, **21**, VI-ES-01, Reykjavík.
- Hubbert, M.K. & Rubey, W.W., 1959. Mechanics of fluid-filled porous solids and its application to overthrust faulting, *Bull. geol. Soc. Am.*, **70**, 115–166.
- Hunt, J.M., 1990. Generation and migration of petroleum from abnormally pressurized fluid compartments, *Am. Assoc. Petrol. Geol. Bull.*, **74**, 1–12.
- Ida, Y., 1972. Cohesive force across the tip of a longitudinal-shear crack and Griffith's specific surface energy, *J. geophys. Res.*, **77**(20), 3796–3805.
- Kanamori, H., 1977. The energy release in great earthquakes, *J. geophys. Res.*, **82**, 2981–2987.
- King, G.C.P., Stein, R.S. & Lin, J., 1994. Static stress changes and the triggering of earthquakes, *Bull. seism. Soc. Am.*, **84**(3), 935–953.
- Linker, M.F. & Dieterich, J.H., 1992. Effects of variable normal stress on rock friction: observations and constitutive equations, *J. geophys. Res.*, **97**(B4), 4923–4940.
- Miller, S.A., Nur, A. & Olgaard, D.L., 1996. Earthquakes as a coupled shear stress-high pore pressure dynamical system, *Geophys. Res. Lett.*, **23**, 197–200.
- Ohnaka, M., 2003. A constitutive scaling law and a unified comprehension for frictional slip failure, shear fracture of intact rocks, and earthquake rupture, *J. geophys. Res.*, **108**(B2), 2080, doi:10.1029/2000JB000123.
- Ohnaka, M. & Yamashita, T., 1989. A cohesive zone model for dynamic shear faulting based on experimentally inferred constitutive relation and strong motion source parameters, *J. geophys. Res.*, **94**(B4), 4089–4104.
- Ohnaka, M., Kuwahara, Y. & Yamamoto, K., 1987. Constitutive relations between dynamic physical parameters near a tip of the propagating slip zone during stick-slip shear failure, *Tectonophysics*, **144**, 109–125.
- Pedersen, R., Sigmundsson, F., Feigl, K.L. & Árnadóttir, T. 2001. Coseismic interferograms of two $M_S = 6.6$ earthquakes in the South Iceland Seismic Zone, June 2000, *Geophys. Res. Lett.*, **28**(17), 3341–3344.
- Powley, D.E., 1990. Pressures and hydrogeology in petroleum basins, *Earth Sci. Rev.*, **29**, 215–226.
- Rice, J.R., 1992. Fault stress states, pore pressure distributions, and the weakness of the San Andreas Fault, in *Fault Mechanics and Transport Properties in Rocks (the Brace Volume)*, pp. 475–503, eds Evans, B. & Wong, T.-F., Academic, San Diego, CA.
- Ripperger, J. & Mai, P.M., 2004. Fast computation of static stress changes on 2D faults from final slip distributions, *Geophys. Res. Lett.*, **31**, L18610, doi:10.1029/2004GL020594.
- Rubin, A.M. & Ampuero, J.-P., 2005. Earthquake nucleation on (aging) rate and state faults, *J. geophys. Res.*, **110**, B11312, doi:10.1029/2005JB003686.
- Ruina, A.L., 1983. Slip instability and state variable friction laws, *J. geophys. Res.*, **88**(B12), 10 359–10 370.
- Rybicki, K., Sato, T. & Kasahara, K., 1985. Mechanical interaction between neighboring active faults: static and dynamic stress field induced by faulting, *Bull. Earthq. Res. Inst. Univ. Tokyo*, **60**, 1–21.
- Scholz, C.H., 2002. *The Mechanics of Earthquakes and Faulting*, 2nd edn, Cambridge University Press, Cambridge.
- Stark, M.A. & Davis, S.D., 1996. Remotely triggered microearthquakes at the Geysers geothermal field, California, *Geophys. Res. Lett.*, **23**, 945–948.
- Stefánsson, R., Gudmundsson, G. & Halldórsson, P. 2003. The South Iceland earthquakes 2000 a challenge for earthquake prediction research, available at: <http://hraun.vedur.is/ja/prepared/SouthIcelandEarthq2000/>, last modified April 2, 2003.
- Vogfjörð, K., 2003. Triggered seismicity after the June 17, $M_w = 6.5$ earthquake in the South Iceland Seismic Zone: the first five minutes, *Geophys. Res. Abstracts*, **5**, 11 251.
- Vogfjörð, K.S. *et al.*, 2002. Crustal profiling in Iceland using earthquake source arrays, *EOS. Trans. AGU*, **83**(45), Fall Meet. Suppl., Abstract S61C 1161.
- Voisin, C., 2002. Dynamic triggering of earthquakes: the nonlinear slip-dependent friction case, *J. geophys. Res.*, **107**(B12), 2356, doi:10.1029/2001JB001121.
- Voisin, C., Campillo, M., Ionescu, I., Cotton, F. & Scotti, O., 2000. Dynamic versus static stress triggering and friction parameters: inferences from the November 23, 1980, Irpinia earthquake, *J. geophys. Res.*, **105**(9), 21 647–21 659.
- Voisin, C., Cotton, F. & Di Carli, S., 2004. A unified model for dynamic and static stress triggering of aftershocks, antishocks, remote seismicity, creep events, and multisegmented rupture, *J. geophys. Res.*, **109**, B06304, doi:10.1029/2003JB002886.
- Zencher, F., Bonafede, M. & Stefánsson, R., 2006. Near-lithostatic pore pressure at seismogenic depths: a thermoporoelastic model, *Geophys. J. Int.*, **166**, 1318–1334.
- Ziv, A., 2006. On the role of multiple interactions in remote aftershock triggering: the Landers and the Hector Mine case studies, *Bull. seism. Soc. Am.*, **96**, 80–89.

APPENDIX A: INTERPOLATION OF THE STRESS PERTURBATION

To have a sufficient spatio-temporal resolution for the fully dynamic code, we develop an algorithm that employs a C^2 cubic spline, often used in seismological applications (e.g. Ripperger & Mai 2004) to interpolate the values of the stress perturbation generated by the June 17 main shock. Quantities $\Delta\sigma_{2i}(x_1, x_3, t)$ ($i = 1, 2, 3$) in Section 2.1 are the results of such an interpolation described below. The C^2 cubic spline is a smooth and one of the most heavily used fourth-order piecewise polynomial functions, that in general are given by (in the univariate case):

$$p(x) = \sum_{r=1}^k c_{rs} \frac{(x - \xi_s)^{r-1}}{(r-1)!}, \quad \text{for } \xi_s \leq x < \xi_{s+1}, \quad (\text{A.1})$$

where k is the order (degree $k-1$) of their polynomial pieces, $\xi \in \mathbb{R}^n$ represents the breakpoint sequence and the $\{c_{rs}\}$ is the $k \times (n-1)$ matrix of their local polynomial coefficients. The breakpoints of the spline are the abscissas, while endpoint conditions are automatically determined by the program. These conditions correspond to the ‘not-a-knot’ condition (see de Boor 1978), which requires that the third derivative of the spline be continuous at the second and next-to-last breakpoint.

Technically, our algorithm proceeds as follows:

1. The original grid of receivers is settled, defining all discrete receivers coordinates on the fault ($x_{1l}^{\text{old}}, x_{3m}^{\text{old}}$), for $l = 1, \dots, l_{\text{end}}; m = 1, \dots, m_{\text{end}}$. In our specific case: $l_{\text{end}} = 12$ and $m_{\text{end}} = 8$.
2. The values of stress perturbations at constant depth (i.e. at constant $x_3^{\text{old}} = x_{3m}^{\text{old}}$ coordinate) are interpolated in the new grid points x_{1i}^{new} giving vectors $\Delta\sigma_{2j}^{\text{new}}(x_{1i}^{\text{new}}, x_{3m}^{\text{old}}, t^{\text{old}})$, $i = 1, \dots, i_{\text{end}}, j = 1, 2, 3$.
3. Values of stress perturbations at constant $x_1^{\text{old}} = x_{1l}^{\text{old}}$ coordinate are interpolated in the new grid points x_{3k}^{new} , giving vectors $\Delta\sigma_{2j}^{\text{new}}(x_{1l}^{\text{old}}, x_{3k}^{\text{new}}, t^{\text{old}})$, $k = 1, \dots, k_{\text{end}}, j = 1, 2, 3$.
4. Values of $\Delta\sigma_{2j}^{\text{new}}(x_{1l}^{\text{old}}, x_{3k}^{\text{new}}, t^{\text{old}})$ determined at point 3 are interpolated in each new point x_{1i}^{new} , giving new vectors $\Delta\tilde{\sigma}_{2j}^{\text{int}(3)}(x_{1i}^{\text{new}}, x_{3k}^{\text{new}}, t^{\text{old}})$, $i = 1, \dots, i_{\text{end}}, k = 1, \dots, k_{\text{end}}, j = 1, 2, 3$.
5. Values of $\Delta\sigma_{2j}^{\text{new}}(x_{1l}^{\text{new}}, x_{3m}^{\text{old}}, t^{\text{old}})$ determined at point 2 are interpolated in each new point x_{3k}^{new} , giving new vectors $\Delta\tilde{\sigma}_{2j}^{\text{int}(1)}(x_{1i}^{\text{new}}, x_{3k}^{\text{new}}, t^{\text{old}})$, $i = 1, \dots, i_{\text{end}}, k = 1, \dots, k_{\text{end}}, j = 1, 2, 3$.
6. The values of the stress perturbations in the new points ($x_{1i}^{\text{new}}, x_{3k}^{\text{new}}$) and at each time t^{old} are simply obtained as the arithmetic average of $\Delta\tilde{\sigma}_{2j}^{\text{int}(1)}$ and $\Delta\tilde{\sigma}_{2j}^{\text{int}(3)}$: $\Delta\sigma_{2j} = \frac{1}{2}(\Delta\tilde{\sigma}_{2j}^{\text{int}(1)} + \Delta\tilde{\sigma}_{2j}^{\text{int}(3)})$, $j = 1, 2, 3$.
7. Points 2 to 6 are iterated for each time levels t^{old} .

Finally, we have to interpolate in time the spatially interpolated value of the stress perturbations, obtained as described above. Also for the temporal interpolation, we use a C^2 cubic spline to obtain the desired temporal discretization $\Delta t = 1.27 \times 10^{-3}$ s. This spatio-temporal discretization satisfies the convergence and stability conditions discussed in BC05. Considering the adopted crustal profile, the eq. (A.4) of BC05 gives $173 \text{ m} = \sqrt{3}\Delta x > v_{F_{\text{max}}}\Delta t = 8.6 \text{ m}$. From eq. (A.5) of BC05, we get that the critical spatial and temporal sampling are $\Delta t^* = \frac{v_{\text{min}}\rho_{\text{min}}L}{4\omega_{\text{CFLmax}}[(b-a)\sigma_n^{\text{eff}}]_{\text{max}}} \cong \frac{v_{\text{min}}\rho_{\text{min}}L}{4\omega_{\text{CFLmax}}(b-a)\sigma_n^{\text{eff}}(x_1, x_3, 0)} = 27.6 \times 10^{-3} \text{ s}$ and $\Delta x^* = \frac{v_{\text{min}}\rho_{\text{min}}L}{4\omega_{\text{CFLmax}}^2[(b-a)\sigma_n^{\text{eff}}]_{\text{max}}} = 1035 \text{ m}$, respectively (in the latter equation ω_{CFL} is the Courant–Friedrichs–Lewy

ratio, which is $\omega_{\text{CFL}} = v_S \Delta t / \Delta x$. In our case, $\omega_{\text{CFLmax}} = 0.04826$). Therefore, both the continuum approximation conditions in (A.6) of BC05 are comfortably satisfied. The discretization used here gives solutions without numerical oscillation due to spatial grid dispersion up to a critical frequency $f_{\text{acc}}^{(s)} = 3.02 \text{ Hz}$, comparable to the maximum frequency at which stress tensor perturbations are calculated (2.78 Hz). Computational efficiency of the numerical code for the solution of the spontaneous problem does not require an (auto) adaptive method for numerical integration and therefore the temporal discretization can be kept constant over the whole simulation.

In Fig. A1, we plot two time snapshots of the distribution on the Hvalhnúkur fault of the along-strike component of the shear stress perturbation before (panels on the left-hand side) and after (panels on the right-hand side) the spatio-temporal interpolation previously described. In Fig. A2, we compare in the 26 s hypocentre (black stars in Fig. A1), the time histories of the perturbations. In Fig. A2(a), we plot the strike component of the shear traction perturbation and in Fig. A2(b), the normal component. We emphasize that the (original) stress values in the black curves of Fig. A2 have been calculated by using the discrete wavenumber and reflectivity code, but these values have not been included in the array of the 96 receivers used for the interpolation. This was to maximize the differences between the original and the new (interpolated) values (red curves in Fig. A2) to test the reliability of the proposed interpolation algorithm. Looking at Figs A1 and A2, we can conclude that all the main features of the stress perturbation field are preserved after the spatio-temporal interpolation, and also the local values in the time series are maintained. A small difference appears in the normal component, but it does not affect the results presented and discussed in this paper.

APPENDIX B: SOLUTION TO THE PROBLEM OF THE INDUCED EXTENDED RUPTURE

In this paper, times are referred to the 2000 June 17 main shock origin time. At time t , in each node of the $x_2 = x_2^f$ fault plane (Σ), we compute the total loads:

$$\mathcal{L}_i = f_{ri} + T_{0i} + \Delta\sigma_{2i} \quad (i = 1 \text{ and } 3). \quad (\text{B.1})$$

In (B.1), T_{0i} are the components of the initial shear traction (described below) and f_{ri} are the components of the load \mathbf{f}_r (namely the contribution of the restoring forces per unit fault area) exerted by the neighbouring points of the fault. Formally $f_{ri} = (M^- f_i^+ - M^+ f_i^-) / [\mathcal{A}(M^+ + M^-)]$, where M^+ and M^- are the masses of the ‘+’ and ‘−’ half split-node of the fault plane Σ (see Fig. 2b) and \mathcal{A} is the split-node area (in this vertical fault case is: $\mathcal{A} = \Delta x_1 \Delta x_3$). From a physical point of view, \mathbf{f}^+ represents the force per unit fault area acting on partial node ‘+’ caused by deformation of neighbouring elements located in the ‘−’ side of Σ (and vice versa for \mathbf{f}^-).

The stress tensor perturbations $\{\Delta\sigma_{2i}\}$ are coupled to the components of the fault friction T_i through the following equations:

$$\begin{aligned} \frac{d^2}{dt^2} u_1 &= \alpha [\mathcal{L}_1 - T_1], \\ \frac{d^2}{dt^2} u_3 &= \alpha [\mathcal{L}_3 - T_3], \end{aligned} \quad (\text{B.2})$$

where $\alpha \equiv \mathcal{A} [(1/M^+) + (1/M^-)]$. The boundary condition here imposed is expressed as $T = \tau$, where T is the modulus of the total shear traction $\mathbf{T}^{(n)}$, acting on the fault ($T = \sqrt{T_1^2 + T_3^2}$, see

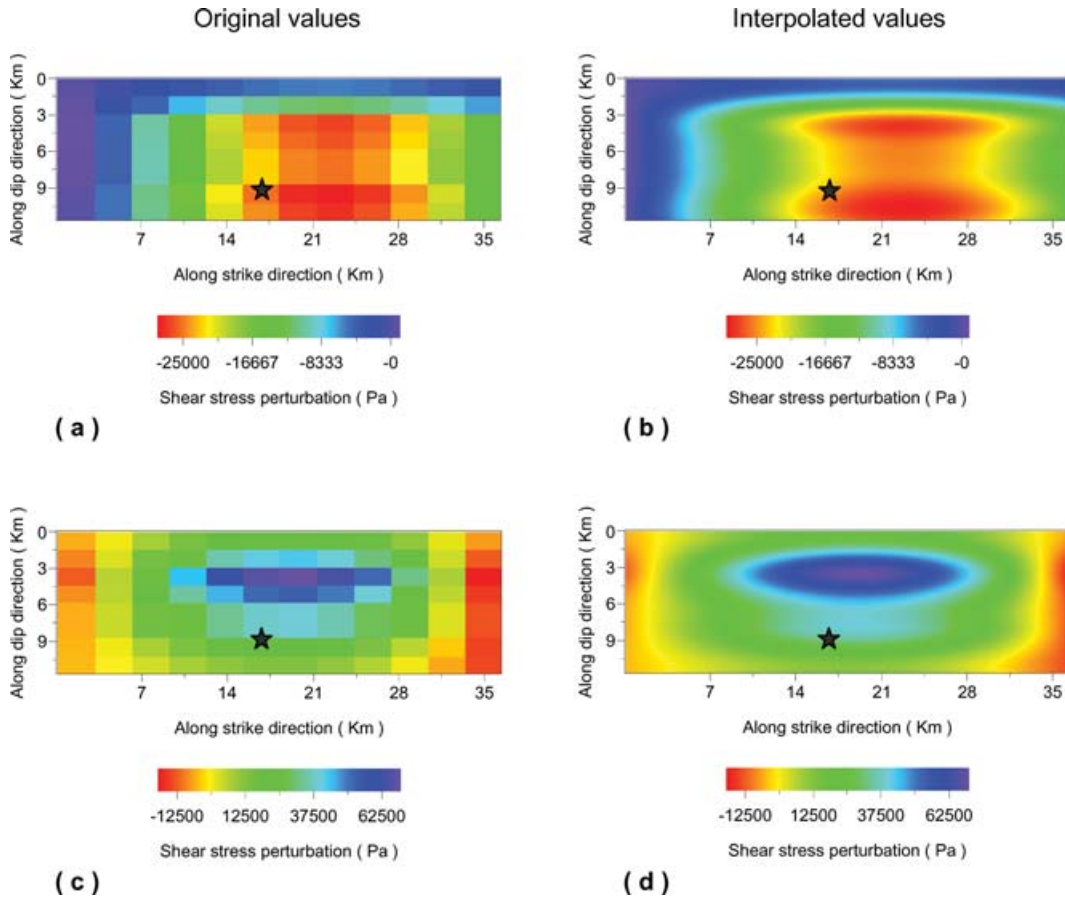


Figure A1. Distribution on the 26 s fault of the shear stress perturbations [namely $\Delta\sigma_{21}(x_1, x_3, t)$] caused by the June 17 main shock. Panels in the left-hand column are the original values calculated at the 96 receivers whereas panels in the right-hand column are the interpolated values in the 42 471 fault points (see Appendix A for the details of the spatio-temporal interpolation algorithm). Panels (a) and (b) are at time $t = 13.18$ s, panels (c) and (d) at time $t = 26.37$ s. The black star is the observed hypocentre of the 26 s event.

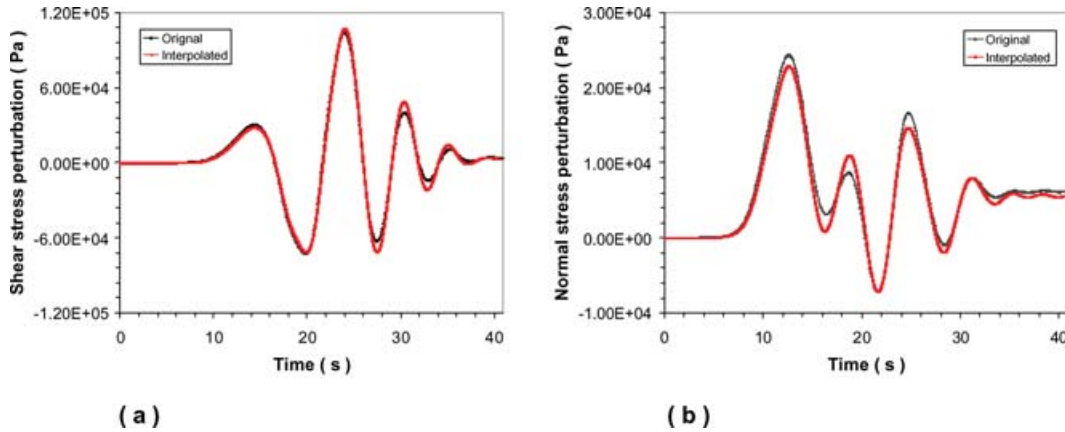


Figure A2. Comparison between the original time series (black curves) and the interpolated time series (red curves) for the perturbation of shear stress (panel a) and normal stress (panel b), namely $-\Delta\sigma_{21}(x_1, x_3, t)$ and $\Delta\sigma_{22}(x_1, x_3, t)$, respectively, in the hypocentre of the 26 s aftershock.

Fig. 2b), and τ is the frictional resistance, which depends on the adopted constitutive relation and is proportional to the effective normal traction acting on the fault. The latter is $\sigma_n^{\text{eff}} = -(\Sigma^{(\hat{n})} \cdot \hat{n} + p_{\text{fluid}})$ where $\Sigma^{(\hat{n})} \cdot \hat{n}$ is the normal stress acting on the solid matrix and p_{fluid} is the pore fluid pressure. At time t , the effective normal

stress is:

$$\sigma_n^{\text{eff}} = -f_{r_2} + \sigma_{n_0}^{\text{eff}} - \Delta\sigma_{22}, \quad (\text{B.3})$$

where $\sigma_{n_0}^{\text{eff}}$ is the initial value of the effective normal stress. The components of the shear pre-stress acting on the fault are

$T_{01} = \tau_0(x_1, x_3) \cos(\varphi_0)$ and $T_{03} = \tau_0(x_1, x_3) \sin(\varphi_0)$, where $\varphi_0 \equiv \varphi(x_1, x_3, 0)$ is the initial azimuth (i.e., the initial rake) and $\tau_0(x_1, x_3)$ is the initial value of friction resistance prescribed by the fault governing law. Taking into account that for our geometry the unit vector normal to Σ is $\hat{\mathbf{n}} \parallel \hat{\mathbf{x}}_2 \equiv (0, 1, 0)$ and that the shear traction is acting on the positive side of Σ , in this case of a right-lateral fault $\varphi_0 = 180^\circ$. Here, as in the BC05 and Bizzarri & Cocco (2006a, b), normal components of the stress tensor are assumed to be negative for compression; note that the opposite notation was used in AEA06.

APPENDIX C: PARAMETRIZATION OF 26 S FAULT

C.1 Fault dimension and seismic moment

The 26 s event produced a small geodetic signal and minor surface effects compared to the 30 s event, suggesting that the rupture area is deep and relatively small (Clifton *et al.* 2003, Árnadóttir *et al.* 2004). Relocated aftershocks of the 26 s event are grouped around two depths—about 4.5 and 8 km (Hjaltadóttir & Vogfjörð 2005; their fig. 12). According to Boatwright and Cocco (1996), Scholz (2002) and De Martini *et al.* (2003), the aftershocks tend to group in the locations where the main rupture produces a stress concentration, that is, around the rupture perimeter where the crack tip is arrested or in almost locked regions of the sliding surface. From the aftershock distribution, we can therefore consider that the seismic part of the fault extends between the depths $x_3 = 5400$ and $x_3 = 7400$ m; we will indicate this depth interval with the symbol \mathcal{I} . The aftershock latitudes are between 63.890°N and 63.951°N (the latitude of the 26 s hypocentre). This latitude interval corresponds to $x_1 \in [9700, 16500]$ m in our local Cartesian reference system $Ox_1x_2x_3$. A vertical alignment of unrelocated aftershocks is observed only in the north end latitude interval. We then define the region $\mathcal{A} = \{\mathbf{x} | x_1 \in [9.7, 16.5] \text{ km}, x_2 = x_2', x_3 [5.4, 7.4] \text{ km}\}$ as a possible candidate of the rupture area, even if, on the basis of the aftershock distribution, its horizontal extent is less constrained than the vertical extent (\mathcal{I}).

We can estimate the static seismic moment of the 26 s event from the well-known relation $\log(M_0) = 1.5M_w + 9$ (Kanamori 1977). Considering an estimated magnitude $M_w \cong 5$ (Vogfjörð 2003; Árnadóttir *et al.* 2006), we obtain M_0 of the order of 3.2×10^{16} N m. This value would increase up to 1.8×10^{17} N m if a moment-magnitude up to 5.5 is assumed (Árnadóttir *et al.* 2004; AEA06). We compare the observed value of M_0 with the value

of the (dynamic) seismic moment $M(t)$, as evaluated at the end of the numerical simulation. The latter is computed as $M(t) = \frac{|\lambda'_1| + |\lambda'_2|}{2}$, where λ'_1 and λ'_2 are two of the three eigenvectors of the (dynamic) seismic moment tensor $\mathcal{M}(t)$, ordered such that $|\lambda'_1| \geq |\lambda'_2| \geq |\lambda'_3|$ (e.g. Dziewonski *et al.* 1981). For our pure double couple geometry it is: $M(t) = \sqrt{M_{21}(t)^2 + M_{23}(t)^2}$, where

$$M_{2i}(t) = \int_{\text{df}} u_i \quad i = 1, 2, \quad (\text{C.1})$$

where G is the depth-variable rigidity modulus and u_1 and u_3 are fault slip components.

C.2 Initial effective normal stress

The effective normal stress acting at $t = 0$ on the 26 s fault plane is assumed to vary only with depth [$\sigma_n^{\text{eff}}(x_1, x_3, 0) = \sigma_{n_0}^{\text{eff}}(x_3)$] since it is evaluated as the difference existing between the lithostatic pressure $\hat{p}^{(\text{litho})}(x_3)$ decreased by the normal component $\Delta\sigma^{(\text{dev})}$ of a deviatoric stress field of tectonic origin and the pore fluid pressure $p_{\text{fluid}}(x_3)$: $\sigma_n^{\text{eff}}(x_3) = \hat{p}^{(\text{litho})}(x_3) - \Delta\sigma^{(\text{dev})} - p_{\text{fluid}}(x_3)$. From Anderson's theory and for our parameters we estimate an average value $\Delta\sigma^{(\text{dev})} = 5.7$ MPa. The lithostatic pressure was computed as $\hat{p}^{(\text{litho})}(x_3) = \hat{\rho}_{\text{rock}} g x_3$, $\hat{\rho}_{\text{rock}}$ being the weighed averaged cubic mass rock density (using the relation $\hat{\rho}_{\text{rock}} \equiv \sum_{k=1}^4 \rho_{\text{rock}k} \frac{x_{3k} - x_{3k-1}}{x_{34} - x_{30}}$, with $x_{30} \equiv 0$) and g , the acceleration due to gravity.

At shallow depths ($x_3 \leq x_3^*$), the pore fluid pressure is assumed to be hydrostatic, $p_{\text{fluid}}^{(\text{hydro})}(x_3) = g \int_0^{x_3} \rho_{\text{fluid}}(x'_3) dx'_3$, where at each depth, the fluid density (Table C1) is calculated iteratively (assuming constant fluid density in each 1 km depth-interval) by using a reasonable temperature profile in Iceland (e.g. Beblo & Björnsson 1980; Hersir *et al.* 1984) and extracting $\rho_{\text{fluid}}(x_3)$ from pressure–temperature tables of Haar *et al.* (1984). For $x_3 \geq x_3^* + D^*$, we assume near-lithostatic pore fluid pressure values $p_{\text{fluid}}^{(nl)}(x_3)$, giving $\sigma_n^{\text{eff}}(x_3) = \sigma_n^{\text{eff}*} = 2.5$ MPa, as in AEA06. We recall here that Hubbert & Rubey (1959) observed that water, provided by dehydration reactions, can exist at near-lithostatic pressures and consequently shear fracturing can occur at very low shear stress. More recently, the over-pressurized fluids are of particular interest in studies related to oil reservoir partitions (Hunt 1990; Powley 1990), as well as to larger-scale crustal processes such as the reduction of strength of mature faults and the earthquake cycles (Byerlee 1990, 1993; Rice 1992; Miller *et al.* 1996). High values of pore fluid pressure are also suggested by Crampin *et al.* (2002), who studied the

Table C1. Temperature and pore fluid pressure distributions on the fault plane (see Appendix Section C2 for details).

Layer no. k	Overpressure $(\hat{p}^{(\text{litho})} - p_{\text{fluid}}^{(\text{hydro})})_k$ (MPa)	Temperature T_k^f (°C)	Fluid density $\rho_{\text{fluid}k}$ (kg m ⁻³)	Depth of x_{3k} (km)
1	0.10	5.00	999.99	0
2	18.8	95.0	970.46	1
3	38.1	185	914.40	2
4	58.7	275	818.45	3
5	82.0	365	716.70	4
6	107	455	633.05	5
7	134	545	541.20	6
8	162	635	485.50	7
9	190	725	465.30	8
10	215	745	491.50	9

polarization of shear wave splitting data recorded in a seismically active area in northern Iceland.

Accordingly, we assume a transitional region of vertical width D^* where pore fluid pressure varies from hydrostatic to near-lithostatic values in agreement with numerical results of Zencher *et al.* (2006), who modelled the behaviour of pore fluid pressure migrating from a reservoir at lithostatic pressure towards the Earth's surface after the rupture of an impermeable barrier of thickness D^* . We associate $x_3^* + D^*$ with the brittle–ductile transition depth, which is around 8 km in the SISZ (Árnadóttir *et al.* 2006; see their fig. 13 with the related discussion and AEA06). On the other hand, we believe that the 26 s rupture developed above the brittle–ductile transition and then within the transitional region ($x_3^* < x_3 < x_3^* + D^*$). Therefore, looking at the aftershock depth distribution discussed in Appendix Section C.1, we assume a thickness $D^* = 3$ km (a reasonable value also proposed by Zencher *et al.* 2006) and $x_3^* = 5800$ m. In particular, we consider a pore fluid pressure that increases with depth towards near-lithostatic values within a narrow region located in the upper part of the transitional region and having an ‘extent on’ the order of h^* ($0 \leq h^* < D^*$). The profile of the initial effective normal stress generated by such a pore fluid pressure (see profile number 3 in Fig. 4b) is expressed by:

$$\sigma_{n_0}^{\text{eff}} = \sigma_n^{\text{eff}} \left(1 - e^{-\frac{x_3 - x_3^*}{h^*}} \right) + \Delta P_2 e^{-\frac{x_3 - x_3^*}{h^*}}, \quad x_3^* < x_3 < x_3^* + D^*, \quad (\text{C.2})$$

where $\Delta P_2 \equiv \hat{p}^{(\text{litho})}(x_3^*) - \Delta \sigma^{(\text{dev})} - p_{\text{fluid}}^{(\text{hydro})}(x_3^*) [p_{\text{fluid}}^{(\text{hydro})}(x_3^*) = 48.02$ MPa is the resulting fluid pressure at $x_3^* = 5800$ m]. In eq. (C.2), h^* is a free parameter that was tuned using the results of different forward dynamic models of the triggered event. A homogeneous value of effective normal stress $\sigma_{n_0}^{\text{eff}}(x_3) = \sigma_n^{\text{eff}*}$ within the transitional region can be obtained from (C.2) by assuming $h^* = 0$ (profile number 1 in Fig. 4b).

APPENDIX D: DETERMINATION OF THE FRICTIONAL PARAMETER OF THE NON-LINEAR SLIP-WEAKENING GOVERNING LAW (EQ. 3)

Looking at Fig. 7(c), in the ‘virtual’ hypocentre, we can estimate the following parameters—an upper yield strength $\tau_u^{\text{eq}} = 2.62$ MPa, a frictional level $\tau_f^{\text{eq}} = 2.01$ MPa, a hardening distance $d_h = 3.31 \times 10^{-4}$ m and a slip-weakening parameter $d_0^{\text{eq}} = 2.05 \times 10^{-2}$ m. The latter gives a ratio $d_0^{\text{eq}}/L = 20.5$, confirming also results obtained for a single fault with a homogeneous rheology (Cocco & Bizzarri 2002; Bizzarri & Cocco 2003, 2006b). Considering that $\tau_u^{\text{eq}} = \mu_u \sigma_n^{\text{eff}}$ and $\tau_f^{\text{eq}} = \mu_f \sigma_n^{\text{eff}}$, we obtain: $\mu_u = 0.742$ and $\mu_f = 0.569$. In eq. (3) we set $d_0 = d_0^{\text{eq}}/5$ and, by definition, the parameters α_{OY} and β_{OY} are determined by simultaneously solving the two transcendental equations:

$$\left. \frac{d}{du} \tau \right|_{u=d_h} = 0, \quad (\text{D.1})$$

$$\tau(u = d_h) = \tau_u^{\text{eq}}. \quad (\text{D.2})$$

Numerical solutions of (D.1) and (D.2) are: $\alpha_{\text{OY}} = 0.115634$ and $\beta_{\text{OY}} = 1.31289 \times 10^{-5}$ m. The choice of $d_0 = d_0^{\text{eq}}/5$ guarantees that the level of kinetic friction τ_f^{eq} is reached when the cumulative slip is about 2.05×10^{-2} m (as in the case of DR law; see Fig. 7c in the main text), nearly equal to $12d_h$ (in agreement with laboratory observations of Ohnaka *et al.* 1987; their figs 5a and 6a). We uniformly apply to all fault points the above-mentioned values for the constitutive parameters α_{OY} , β_{OY} , d_0 and μ_f . On the contrary, $\tau_0(x_1, x_3)$ has been set to be exactly equal to that used in cases B and C presented in the main text, and therefore it is variable with depth.